

A two characteristic length nonlocal GTN model: application to cup–cone and slant fracture

A. El Ouazani Tuhami^a, S. Feld-Payet^b, S. Quilici^c, N. Osipov^c, J. Besson^a

^a*MINES ParisTech, PSL Research University, Centre des Matériaux, CNRS UMR 7633, 91003
Evry — France*

^b*DMAS, ONERA, Université Paris Saclay, F-92322 Châtillon — France*

^c*Transvalor, S.A. 950 avenue Roumanille - CS 40237 Biot - 06904 Sophia Antipolis cedex —
France*

Abstract

Ductile failure prediction is essential to avoid loss of structural integrity or to control crack propagation during forming processes. One of the main difficulties is the prediction of complex crack paths. This study proposes a nonlocal extension of a local Gurson-Tvergaard-Needleman (GTN) ductile damage model at finite strains able to capture cup–cone or slant fracture. The proposed model is based on an implicit gradient formulation which enables to solve the problem of spurious strain and damage localization. The model integrates two different material characteristic lengths, which are used to separately regularize damage by void growth and damage by damage nucleation. After parameter fitting using data for a line pipe steel, conditions to obtain converged solutions are studied, which can be used to select the mesh size in the localization band. With the appropriate mesh design, it was possible to study the effect of the characteristic lengths on the formation of cup–cone fracture and slant fracture. It is observed that, for a given specimen size, larger characteristic lengths favor flat crack advance. Similarly, for given material lengths, size effects can be predicted with small specimens being more prone to flat fracture. This paves the way to a more direct determination of material lengths by using homothetic specimens so as to obtain different crack paths.

Keywords: Nonlocal GTN model; Characteristic length; Ductile failure; Cup cone fracture; Slant fracture;

*Corresponding author

URL: jacques.besson@mines-paristech.fr (J. Besson)

1. Introduction

Predicting ductile failure is a major challenge when trying to prevent catastrophic failure of structures or to control crack propagation in the case of metal forming. One of the main challenges is the prediction of complex crack paths in metals such as cup-cone or slant fracture. To achieve this goal, models able to robustly represent the local degradation phenomena (damage nucleation, growth and coalescence) are needed. Among such models is the micro-mechanics based Gurson–Tvergaard–Needleman (or GTN) model (Tvergaard and Needleman, 1984). Based on this seminal framework, numerous extensions have been proposed, which are reviewed *e.g.* in (Tvergaard, 1990; Besson, 2009; Benzerga and Leblond, 2010; Pineau et al., 2016). They are able to account for void shape, void orientation, plastic anisotropy, strain rate sensitivity, coalescence by internal necking...

All these models must lead to softening up to a point where the material entirely loses its load-carrying capacity so as to be able to model fracture. These softening models were first developed within the usual local framework and thus suffered from the well-known numerical issues such as mesh size and mesh orientation dependence (Rousselier et al., 1989; Liu et al., 1994; Besson et al., 2001). Due to the loss of ellipticity of the equations in statics, the solution to the mechanical problem is no longer unique. Overcoming these issues is fundamental for the reliability of fracture simulations. Using a finite strain framework is also required as ductile fracture is always accompanied by large deformations. Several solutions have been proposed to overcome mesh dependency. A first solution is based on a local enrichment by embedding a finite thickness band (Huespe et al., 2009). In that case, the band is introduced when loss of ellipticity is detected within one element. The normal to the band is determined following Rice’s bifurcation analysis (Rice, 1976). Another solution is based on implicit gradient methods (Peerlings et al., 1996; Geers et al., 1998) which facilitate the use of integral methods as originally proposed in (Pijaudier-Cabot and Bazant, 1987; Bazant and Pijaudier-Cabot, 1988). These methods have been used to model ductile fracture for metals within a finite strain framework (Enakoutsa et al., 2007; Mediavilla et al., 2006; Linse et al., 2012; Hütter et al., 2013; Javani et al., 2016; Seupel et al., 2020; Leclerc et al., 2020) although they were initially developed for quasi-brittle failure. Using an implicit gradient formulation, the local constitutive equations are preserved at the cost of small adaptations. This

makes this formulation particularly attractive in the case of the GTN model, as its initial micro-mechanical foundations are then preserved. Multiple internal lengths were introduced in (Nguyen et al., 2020). This model uses an implicit gradient formulation written in the initial configuration. An internal length was associated with each damage evolution mechanism: (i) void growth based on the classical GTN model, (ii) internal necking governed by a heuristic extension of the Thomason model (Thomason, 1985b,a) based on the maximum principal stress, (iii) shear-dominated coalescence mechanisms controlled by the maximum shear stress (Torki et al., 2015). Although the model proposes different internal length scales, the same characteristic length was assigned to the three nonlocal variables in the presented simulations. Micromorphic models (Forest, 2009) can also be used to solve problems related to the loss of ellipticity. They use local state variables and their “micromorphic” counterparts. The free energy of the system depends on the gradient of the micromorphic variables and on coupling terms. Ductile fracture was modeled using this class of models in (Brepols et al., 2017; Diamantopoulou et al., 2017). In particular, models based on a microdilatational theory (Huetter, 2017) appear to be well suited to represent ductile damage by void growth. More recently, nonlocal gradient enhanced energy (GEE) models, first developed for quasi-brittle fracture (Lorentz and Andrieux, 1999) were also used to model ductile failure (Zhang et al., 2018; Chen et al., 2020). They only use the gradient of a local state variable. A decomposition—coordination technique is used to treat the non-locality. The variable of interest is duplicated: a first instance is used at the (global) scale of the structure while a second instance is used at the (local) constitutive law level. As both variables represent the same field, they should be equal. A Lagrange multiplier is introduced to ensure this equality weakly. Finally, the regularization of ill-posed problems can also be achieved by coupling the elastoplastic models with phase-field formulations. This type of formulation was initially introduced for brittle failure (Francfort and Marigo, 1998; Hofacker and Miehe, 2012; Miehe et al., 2010; Heider and Markert, 2017). However, many extensions to ductile fracture have been introduced for 2D simulations (Ambati et al., 2015; Aldakheel et al., 2018), for 3D simulations (Aldakheel et al., 2018; Ambati et al., 2016; Borden et al., 2016; Miehe et al., 2015, 2016; Hu et al., 2021) and also for 3D simulations with remeshing techniques (Eldahshan et al., 2021). More recently, a porous ductile model using a phase-field formulation was introduced in which the critical energy is decomposed into elastic and plastic contributions where the plastic part is described using a GTN model (Dittmann et al., 2020).

This work proposes a nonlocal extension of the GTN material model (based on

(Besson et al., 2001, 2003)) using an implicit gradient framework incorporating two nonlocal characteristic lengths to capture complex ductile failure patterns, such as cup–cone or slant crack paths. The most common issue with nonlocal formulations is the choice of the characteristic lengths. In this paper, comparisons with experimental data on steel specimens first enable obtaining an order of magnitude for the model parameters. Then two length scales are distinguished in the model to account for the different spacings that exist between material defects responsible for damage nucleation and void growth. In the case of ferritic steels used in modern pipelines, two damage mechanisms exist: (i) void growth from MnS and oxides and (ii) damage nucleation at iron carbides (Fe_3C), which occurs at high strains. MnS and oxides early debond from the metallic matrix so that they can be considered as initial voids. Similar damage behavior is *e.g.* observed in aluminum alloys where coarse particles are Fe–rich inclusions and small particles are strengthening dispersoids (Bron et al., 2004). In order to guide the choice of these characteristic lengths, an original study is conducted on their effect on the occurrence of cup-cone and slant fracture.

This work is structured as follows. First, in section 2, the local version of the model is briefly recalled, and its nonlocal modification is introduced. The proposed finite strain formulation is also introduced within an updated Lagrangian framework. In section 3, a parameter fit is carried out for both the local and nonlocal versions of the GTN model based on existing literature data. In section 4, the independence of the results to both mesh size and mesh orientation is checked using the same characteristic length for both mechanisms. The relationship between the numerically obtained localization band width and the characteristic lengths is also investigated. This allows the selection of appropriate mesh sizes for given characteristic lengths. Finally, in section 6, an investigation is presented of the effect of different characteristic lengths for damage nucleation and void growth on the formation of cup-cone, and slant crack paths and the results are translated in terms of size effects.

2. Material models and their framework

In the first part of this section, the local version of the considered GTN model used throughout the paper is briefly recalled. From this basis, the proposed modifications to obtain a nonlocal model with two characteristic lengths are developed. A corotational finite strain formulation is used to deal with large strains (see section 2.2). This allows to use a simple small strain like formulation

for the constitutive model based on an additive strain decomposition of the strain tensor.

2.1. Material models

The used local model is based on the GTN model presented by [Besson et al. \(2001\)](#) but with a different nucleation function using the accumulated plastic strain κ as opposed to the original model which uses the growth porosity f_g .

2.1.1. Local GTN model

One assumes the additive decomposition of the strain tensor (ε) into an elastic (ε_e) and a plastic (ε_p) part. The elastic strain tensor and the stress tensor are related using Hooke's law:

$$\boldsymbol{\sigma} = \mathbb{E} : \varepsilon_e \quad (1)$$

where \mathbb{E} is the fourth-order elasticity tensor. Work hardening is assumed to be isotropic, and the flow stress of the sound material ($R(\kappa)$) is expressed as a function of the accumulated plastic strain κ assuming a power law:

$$R(\kappa) = K(e_0 + \kappa)^n \quad (2)$$

e_0 , K and n are parameters to be identified (any other function could indeed be used). The yield surface is then expressed following [Besson et al. \(2001\)](#) as:

$$\Phi = \sigma_\star - R(\kappa)$$

where σ_\star is an effective stress measure depending on both the stress tensor and the void volume fraction, which is the only damage parameter. In the case of the GTN model, the effective scalar stress is implicitly defined as:

$$G(\boldsymbol{\sigma}, f, \sigma_\star) = \frac{\sigma_{eq}^2}{\sigma_\star^2} + 2q_1 f_\star \cosh\left(\frac{q_2}{2} \frac{\sigma_{kk}}{\sigma_\star}\right) - 1 - q_1^2 f_\star^2 \stackrel{\text{def}}{=} 0 \quad (3)$$

where σ_{eq} is the von Mises stress invariant¹ of the Cauchy stress, σ_{kk} designates its trace, q_1 and q_2 are two parameters and f_\star is a function of porosity. Function f_\star is defined as in ([Tvergaard and Needleman, 1984](#)):

$$f_\star = \begin{cases} f & \text{if } f \leq f_c \\ f_c + \delta(f - f_c) & \text{otherwise} \end{cases} \quad (4)$$

¹Note that the model can be easily extended to plastically anisotropic materials by replacing the von Mises by any stress measure accounting for anisotropy ([Benzerga and Besson, 2001](#); [Tanguy et al., 2008](#); [Shinohara et al., 2016](#)).

where f_c represents the porosity at the onset of void coalescence and $\delta \geq 1$ is a parameter which represents the increased deleterious effect of porosity above f_c . The damage variable f can be itself decomposed into two parts which reflect the fact that damage is caused by damage nucleation (f_n) and void growth (f_g), so that the total damage is equal to $f = f_g + f_n$. The evolution of these damage variables is given by the following set of equations:

$$\dot{f}_g = (1 - f_g)\text{trace}(\dot{\epsilon}_p) \quad \text{mass conservation} \quad (5)$$

$$\dot{f}_n = A_n(\kappa)\dot{\kappa} \quad \text{strain controlled nucleation} \quad (6)$$

where A_n is a coefficient representing the damage nucleation rate. It is expressed as a function of κ so as to represent strain-controlled nucleation (Chu and Needleman, 1980; Zhang et al., 2000). Note that eq. 5 slightly differs from the original one where $(1 - f_g - f_n)$ is used and not $(1 - f_g)$. As MnS inclusions early debond from the matrix, it is unnecessary to describe the nucleation of voids on these inclusions. In this work, nucleation corresponds to damage created on iron carbides which are much smaller than the MnS inclusions. It is assumed that this creates very small voids but high damage. For that reason, the equation for \dot{f}_g is modified as growth is only attributed to large voids originated at MnS inclusions. In practice, this modification has little effect on the overall behavior. The plastic strain rate tensor $\dot{\epsilon}_p$ is obtained using the normality rule:

$$\dot{\epsilon}_p = (1 - f)\dot{\kappa} \frac{\partial \Phi}{\partial \boldsymbol{\sigma}} = (1 - f)\dot{\kappa} \frac{\partial \sigma_\star}{\partial \boldsymbol{\sigma}} = (1 - f)\dot{\kappa} \mathbf{n} \quad (7)$$

where \mathbf{n} designates the normal to the yield surface. Using this expression, the following equivalence between the macroscopic (left handside) and the microscopic (right handside) plastic dissipations is obtained as:

$$\dot{\epsilon}_p : \boldsymbol{\sigma} = (1 - f)\dot{\kappa}\sigma_\star \quad (8)$$

as σ_\star is an homogeneous function of order 1 of $\boldsymbol{\sigma}$.

It is assumed that the considered material can exhibit a slight strain rate dependence, so that $\dot{\kappa}$ is expressed as:

$$\dot{\kappa} = \mathcal{F}(\Phi) = \dot{p}_0 \left\langle \frac{\sigma_\star - R}{\sigma_0} \right\rangle^n \quad (9)$$

where $\langle \cdot \rangle$ is the positive part function and n , \dot{p}_0 and σ_0 are material parameters.

2.1.2. Nonlocal GTN model

The proposed extension of this GTN model uses the implicit gradient methodology proposed in (Peerlings et al., 1996; Geers et al., 1998; Engelen et al., 2003) to regularize two state variables: the volume variation $\omega = \text{trace}(\epsilon_p)$ and the effective accumulated plastic strain κ . Their nonlocal counterparts are referred to as $\bar{\omega}$ and $\bar{\kappa}$. Their evolution within the considered material body Ω is governed by the following Helmholtz-type equations:

$$\bar{\omega} - l_\omega^2 \Delta \bar{\omega} = \omega \quad \text{in } \Omega \quad (10)$$

$$\bar{\kappa} - l_\kappa^2 \Delta \bar{\kappa} = \kappa \quad \text{in } \Omega \quad (11)$$

with the following natural boundary conditions:

$$\vec{\nabla} \bar{\omega} \cdot \vec{n} = 0 \quad \text{on } \partial\Omega \quad (12)$$

$$\vec{\nabla} \bar{\kappa} \cdot \vec{n} = 0 \quad \text{on } \partial\Omega \quad (13)$$

where $\partial\Omega$ and \vec{n} respectively designate the boundary of the body Ω and its outer normal vector.

Let us note that the gradients are calculated on the current configuration and not on the initial configuration as considered by (Leclerc et al., 2020; Nguyen et al., 2020). Besides, this model introduces two characteristic lengths in equations 10 and 11, l_ω and l_κ , respectively associated to void growth and nucleation mechanisms.

The nonlocal variables $\bar{\omega}$ and $\bar{\kappa}$ are then used to formulate the evolution of the damage variables f_g and f_n as:

$$\dot{f}_g = (1 - f_g) \dot{\bar{\omega}} \quad (14)$$

$$\dot{f}_n = A_n(\bar{\kappa}) \dot{\bar{\kappa}} \quad (15)$$

These two equations now replace equations 5 and 6. All other equations remain unchanged. In particular, the hardening law $R(\kappa)$ remains identical, which would not be the case with micromorphic models (Forest, 2009) or gradient enhanced energy models (Chen et al., 2020) as it is expressed as a function of $\bar{\kappa}$ in those cases. In the present case, the flow stress then remains unaffected by the gradient of κ .

2.1.3. Implicit local resolution

The state variables describing the material behavior are then the elastic strain tensor (ϵ_e), the accumulated plastic strain (κ), the porosity due to void growth

(f_g), the porosity due to damage nucleation (f_n) and the volume variation ω . Their evolution laws can be expressed as functions of the rates of the input variables $\dot{\epsilon}$, $\dot{\bar{\omega}}$, $\dot{\bar{\kappa}}$ as:

$$\dot{\epsilon}_e = \dot{\epsilon} - (1 - f_g)\dot{\kappa}\mathbf{n} \quad (16)$$

$$\dot{\kappa} = \mathcal{F}(\Phi) \quad (17)$$

$$\dot{f}_g = (1 - f_g)\dot{\bar{\omega}} \quad (18)$$

$$\dot{f}_n = A_n\dot{\bar{\omega}} \quad (19)$$

$$\dot{\omega} = \text{trace}((1 - f_g)\dot{\kappa}\mathbf{n}) = (1 - f_g)\dot{\kappa}\text{trace}(\mathbf{n}) \quad (20)$$

The implicit resolution of this system of equations for each integration point, detailed in [Appendix A](#), requires its integration over a finite time step Δt . This leads to a system of equations relating the residuals of these equations to the increments of the state variables $\Delta \mathbf{V}_S = (\Delta \epsilon_e, \Delta \kappa, \Delta f_g, \Delta f_n, \Delta \omega)$, for a given set of the increments of input variables $\Delta \mathbf{V}_{IN} = (\Delta \epsilon, \Delta \bar{\omega}, \Delta \bar{\kappa})$. The resolution of this system directly gives the increments of output variables $\Delta \mathbf{V}_{OUT} = [\Delta \sigma, \Delta \omega, \Delta \kappa]$. It then becomes possible to numerically compute the consistent tangent matrix by considering that any given small variation of the input variables $\delta \mathbf{V}_{IN}$ leads to a modification of the state variables so that the residual equations remain null (see details in [Appendix B](#)). The consistent tangent matrix can be expressed as a block-matrix as:

$$\mathbf{K}^{\text{mat}} = \frac{\partial \Delta \mathbf{V}_{OUT}}{\partial \Delta \mathbf{V}_{IN}} = \begin{pmatrix} \frac{\partial \Delta \sigma}{\partial \Delta \epsilon} & \frac{\partial \Delta \sigma}{\partial \Delta \bar{\omega}} & \frac{\partial \Delta \sigma}{\partial \Delta \bar{\kappa}} \\ \frac{\partial \Delta \omega}{\partial \Delta \epsilon} & \frac{\partial \Delta \omega}{\partial \Delta \bar{\omega}} & \frac{\partial \Delta \omega}{\partial \Delta \bar{\kappa}} \\ \frac{\partial \Delta \kappa}{\partial \Delta \epsilon} & \frac{\partial \Delta \kappa}{\partial \Delta \bar{\omega}} & \frac{\partial \Delta \kappa}{\partial \Delta \bar{\kappa}} \end{pmatrix} \quad (21)$$

The terms of this matrix are required to express the elementary stiffness matrix of the associated finite elements.

2.2. Finite strain framework

Both local and nonlocal GTN models must be formulated within a finite strain framework. This is done using a rotating frame concept.

Corotational framework. To do so, a corotational formulation ([Sidoroff and Dogui, 2001](#)) is used. The corotational frame is defined using the rotation tensor \mathbf{Q} such that:

$$\dot{\mathbf{Q}} = \mathbf{W} \cdot \mathbf{Q} \quad \text{with} \quad \mathbf{Q}(t = 0) = \mathbf{1} \quad (22)$$

where the \mathbf{W} tensor designates the skew-symmetric part of the velocity gradient tensor \mathbf{L} . The symmetric part of the velocity gradient tensor is denoted \mathbf{D} so that: $\mathbf{L} = \mathbf{D} + \mathbf{W}$. This velocity gradient tensor is defined from the transformation tensor $\mathbf{F} = \partial \vec{x} / \partial \vec{X}$ (where \vec{X} is the position of a material point in the initial configuration and \vec{x} its position in the current configuration) and its derivative as: $\mathbf{L} = \dot{\mathbf{F}} \cdot \mathbf{F}^{-1}$. Knowing the rate of deformation \mathbf{D} , one gets the material deformation rate through the following expression:

$$\dot{\epsilon} = \mathbf{Q}^T \cdot \mathbf{D} \cdot \mathbf{Q} \quad (23)$$

Knowing the corotational Cauchy stress (i.e., the Cauchy stress expressed in the coordinate system that rotates with the material), the Cauchy stress in the unrotated frame is given by:

$$\Sigma = \mathbf{Q} \cdot \sigma \cdot \mathbf{Q}^T \quad (24)$$

Let us note that the rotated rate of σ is the Jaumann rate of Σ .

Finite element formulation. Considering cases where the load is applied sufficiently slowly so that the inertial forces can be neglected, the weak form of the equilibrium equations then reads:

$$\forall \vec{v}^* \int_{\Omega} \Sigma : \mathbf{L}^* d\Omega = \int_{\Omega} \Sigma : \mathbf{D}^* d\Omega = W_{\text{ext}}^*, \quad \text{with } \mathbf{L}^* = \frac{\partial \vec{v}^*}{\partial \vec{x}} \quad (25)$$

where \vec{v}^* is a virtual velocity field, W_{ext}^* represents the virtual power of external forces and \mathbf{D}^* is the symmetric part of \mathbf{L}^* .

In the case of a nonlocal formulation, based on equations 10, 11 and 12, the weak form corresponding to the nonlocal variables is expressed as:

$$\begin{aligned} \forall \dot{\bar{w}}^* \quad & \int_{\Omega} (\bar{w} - w) \dot{\bar{w}}^* + l_w^2 \vec{\nabla} \bar{w} \cdot \vec{\nabla} \dot{\bar{w}}^* d\Omega = 0 \\ \forall \dot{\bar{p}}^* \quad & \int_{\Omega} (\bar{p} - p) \dot{\bar{p}}^* + l_p^2 \vec{\nabla} \bar{p} \cdot \vec{\nabla} \dot{\bar{p}}^* d\Omega = 0 \end{aligned} \quad (26)$$

where $\dot{\bar{w}}^*$ and $\dot{\bar{p}}^*$ designates a virtual rate of the nonlocal field. Gradients are evaluated in the current configuration as $\vec{\nabla} \bullet = \partial \bullet / \partial \vec{x}$.

These equations must then be discretized both in time and in space, as detailed in Appendix C. For the spatial discretization, quadratic shape functions are used for displacement degrees of freedom (DOFs), and linear shape functions are used for the nonlocal variables (The notation P2P1P1 is used in this paper to refer to this choice of interpolation order).

The discretization of the set of equations 25 and 26 leads to a global system built thanks to the assembly of elementary reactions. This system relates the unknown variables to the external forces through the assembly of elementary stiffness matrices. The calculation of the different terms of these elementary matrices requires the evaluation of the consistent tangent matrix \mathbf{K}^{mat} , as detailed in Appendix D. The resolution of this system is performed implicitly using a Newton–Raphson algorithm and leads to the simultaneous determination of the DOFs associated with the displacements and the nonlocal variables (as opposed to a staggered resolution scheme).

3. Fitting of the model parameters

3.1. Model parameters

The constitutive model of (Besson et al., 2001, 2003) being relatively close to the local one presented in this paper, it is possible to use the same elasto–visco–plastic parameters and most of the GTN parameters (see table 1). The low initial porosity (f_0) corresponds to that of a modern line pipe steel. It corresponds to the MnS inclusion volume fraction as these particles easily debond from the matrix.

Table 1: Set of material parameters from (Besson et al., 2001, 2003)

Young modulus	E	210 GPa
Poisson ratio	ν	0.3
Isotropic hardening (power law)	K	795 MPa
	e_0	0.002
	n	0.13
Gurson criterion	q_1	1.5
	q_2	1.
	f_0	$1.5 \cdot 10^{-4}$
Viscosity	\dot{p}_0	1 s^{-1}
	σ_0	55 MPa
	n	5

The main difference between the constitutive model of (Besson et al., 2001, 2003) and the local model in this paper is the damage nucleation rate function $A_n(\kappa)$ in equation 6. In the model described in (Besson et al., 2001, 2003), $A_n(\kappa)$ is a function of the growth porosity f_g , whereas in this paper, this function

is chosen to be a constant (A_n) when the accumulated plastic strain reaches a threshold κ_c :

$$A_n(\kappa) = \begin{cases} A_n & \text{if } \kappa > \kappa_c \\ 0 & \text{otherwise} \end{cases} \quad (27)$$

The model was changed as the initial version did not allow forming cup-cone fracture using the nonlocal formulation. This leaves thus two material parameters, A_n and κ_c , to be fitted. Besides, the nonlocal model requires the identification of the two nonlocal characteristic lengths l_ω and l_κ .

3.2. Tests used for the fit of the nucleation law

The experimental database consists of an axisymmetric tensile test presented in (Besson et al., 2001) and a plane strain test described in (Besson et al., 2003). Both tests were carried out on the same material, i.e., X70 HSLA (high strength low alloyed) ferritic-pearlitic steel, and are experimental results from (Rivalin, 1998). They have been selected because they result in complex crack paths, with cup-cone fracture for the axisymmetric specimen and slant fracture for the plane strain specimen. In addition, the tests have been used in the literature (Scheider and Brocks, 2003; Huespe et al., 2012; Leclerc et al., 2020) as a reference to identify and study ductile fracture models.

Finite element simulations are carried out for both tests in order to fit the parameters (trial and error procedure). Meshes, dimensions as well as boundary conditions are shown in fig. 1a and fig. 1b. Mesh design is similar in both cases. In the case of the plane strain specimen, the entire specimen is meshed to enable the formation of a slanted crack path. In both cases, elements have quadratic shape functions with eight nodes and reduced integration (4 integration points). In the following S_0 represents the initial minimal cross-section of each specimen; $S_0 = \pi/4\phi_0^2$ for the axisymmetric specimen (with ϕ_0 the initial diameter at the center of the specimen); $S_0 = e_0w_0$ for the plane strain specimen where e_0 represents the specimen thickness and w_0 the width of the specimen. The normalized force (F/S_0) is then plotted as a function of the minimum diameter variation ($\Delta\Phi/\Phi_0$) or thickness variation ($\Delta e/e_0$).

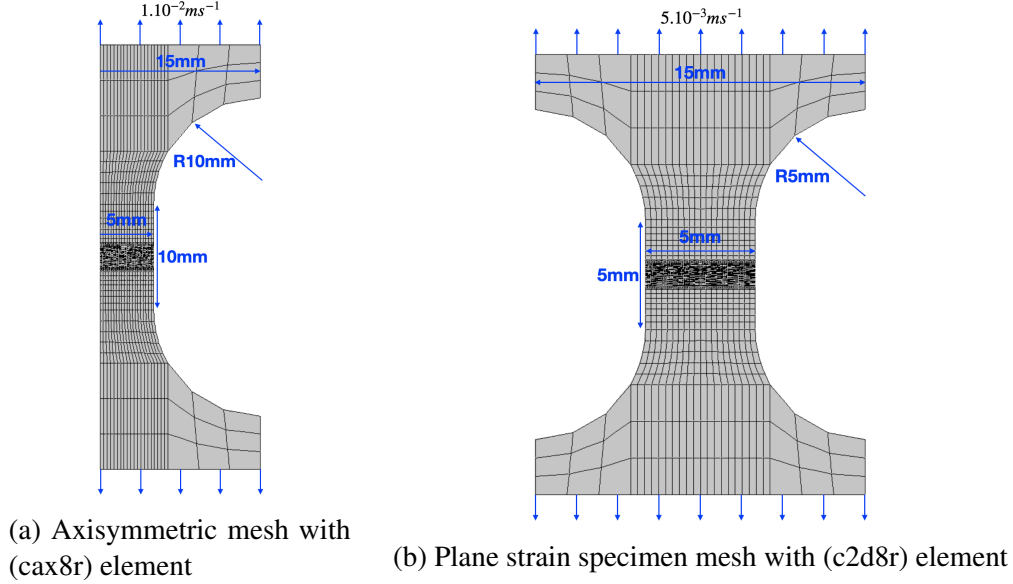


Figure 1: Dimensions and boundary conditions for the tensile test simulations of the axisymmetric specimen 1a and the plane strain specimen 1b.

3.3. Parameter fit for the local model

In the case of local models, it is important to keep the same mesh size in areas where cracks propagate (Liu et al., 1994; Skallerud and Zhang, 1999). Because the diameter of the tensile bar (10 mm) is twice the thickness of the plane stress specimen (5 mm) and because symmetry is not accounted for in the latter case, the same number of elements (N_h) is used to discretize the minimum cross-sections in order to keep the same mesh size. The initial aspect ratio of these elements (r_h) is set to 6:1 so that it leads to approximately square elements at the onset of fracture. Using $N_h = 60$, the initial mesh size is consequently: $83\mu\text{m} \times 14\mu\text{m}$.

The fitted material parameters are:

$$A_n = 0.2 \quad \text{and} \quad \kappa_c = 1.2 \quad (28)$$

Indeed, using these values, the global responses for both test cases show a good agreement with both reference results, as can be seen in fig. 2. In the case of the axisymmetric specimen (figure 2a), it can be noted that the fitted local model response is identical to the reference one before crack initiation, which corresponds to the sharp load drop. In this regime, the damage has minimal effect on the overall behavior. Crack initiation occurs at a slightly higher diameter

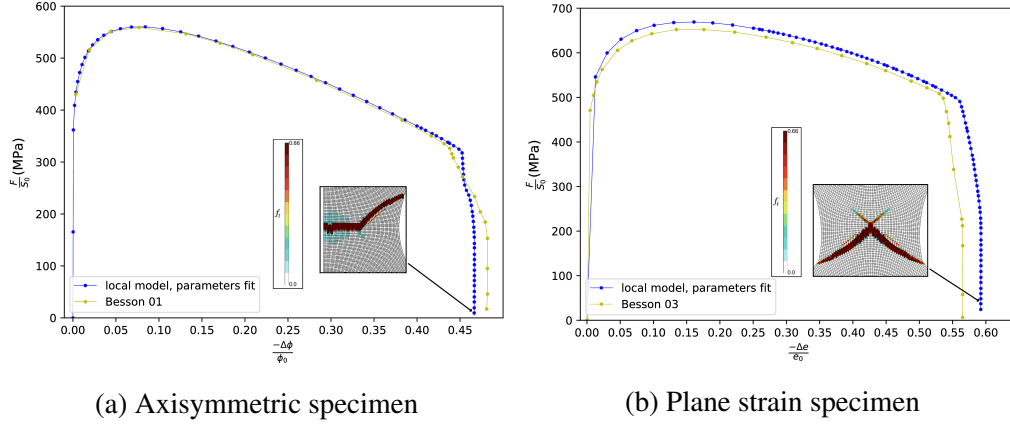


Figure 2: Evolution, for the local model, of the engineering stress as a function of the diameter reduction $-\Delta\phi/\phi_0$ for the axisymmetric specimen (left) and the thickness reduction $-\Delta e/e_0$ for the plane strain specimen (right). The comparison with global curves from the literature (respectively from (Besson et al., 2001) and (Besson et al., 2003)) indicates a correct parameter fit. Total porosity is displayed at total failure for both simulations: a cup-cone failure (left) and a slant failure (right) can be respectively observed.

reduction ($-\Delta\phi/\phi_0 = 0.453$) compared to the reference ($-\Delta\phi/\phi_0 = 0.44$). Besides, as load drop is faster for the new fitted parameters, the total diameter reduction $(-\Delta\phi/\phi_0)_c = 0.467$ is ultimately slightly smaller than in the case of the reference simulation $(-\Delta\phi/\phi_0)_c = 0.48$. The difference is less than 3 % and is acceptable. As can be seen on the image of total porosity at the end of the simulation (fig. 2a), a cup-cone crack path is obtained.

In the case of the plane strain specimen (fig. 2b), the computed forces before crack initiation are slightly higher than the reference ones. This can be explained by the fact that in the reference simulation (Besson et al., 2003), a Hill anisotropic model was used to describe plasticity. Such behavior is not accounted for in the present material model. In this case too, the thickness reduction $(-\Delta e/e_0)_c = 0.59$ predicted using the new model parameters is slightly different from the reference $(-\Delta e/e_0)_c = 0.566$. As in the case of the tensile test, the difference is acceptable. As can be seen on the image of total porosity at the end of the simulation (fig. 2b), a V-shaped crack path is obtained. Note that both V-shaped and S-shaped crack paths can be experimentally obtained (Besson et al., 2013).

3.4. Parameter fit for the nonlocal model

Using the local model, the band width is about the element height in the deformed configuration. For the above-considered cases, this size is $l_b^{local} \approx$

Table 2: Material parameters for the local and nonlocal models.

	local model	nonlocal model
κ_c	1.2	1.2
A_n	0.2	0.4
$l_\kappa = l_\omega$	—	$40\mu\text{m}$

$70\mu\text{m}$. The characteristic length for the nonlocal model was then selected so that the resulting band width (l_b^{nl}) is approximatively equal to l_b^{local} . It is therefore assumed that the mesh size for the local model allows representing the material's internal length following the early work by [Rousselier \(1987\)](#). Having $l_b^{nl} \approx l_b^{local}$ is a simple way to establish a correspondence between both models. It is shown below (section 5.3) that the band width is related to the nonlocal characteristic length by the following relation: $l_b^{nl} \approx 1.5l_c$. Using this relation, one gets $l_\omega = l_\kappa \approx 40\mu\text{m}$. Using these values, 90 elements are required to discretize the specimen radius or thickness with at least three elements in the band width. Using fewer elements results in simulations being mesh dependent. This results in an initial element height equal to $10\mu\text{m}$. As for the damage nucleation rate parameter A_n , since the nonlocal model will always lead to higher ductilities than the local model for a given set of material parameters, it was necessary to impose a larger value: $A_n = 0.4$. Nucleation parameters for the local and nonlocal models are compared in table 2. Note that the number of elements used to mesh the minimum cross-section differs using the above hypotheses. Using $N_h = 60$ for the nonlocal model would result in slightly mesh-dependent simulations.

This fit leads to a relatively good agreement of the global responses for both test cases with the reference results as well as results from the literature ([Huespe et al., 2012](#); [Leclerc et al., 2020](#)), as can be seen in figures 3 and 4. For the simulation of the smooth axisymmetric bar (see figure 3), the engineering stress—diameter reduction curve is particularly close to the reference from ([Besson et al., 2001](#)), and the total failure diameter reduction is well predicted. As can be seen in the images of total porosity taken at different stages of the simulation in the same figure, a cup–cone crack path is also obtained.

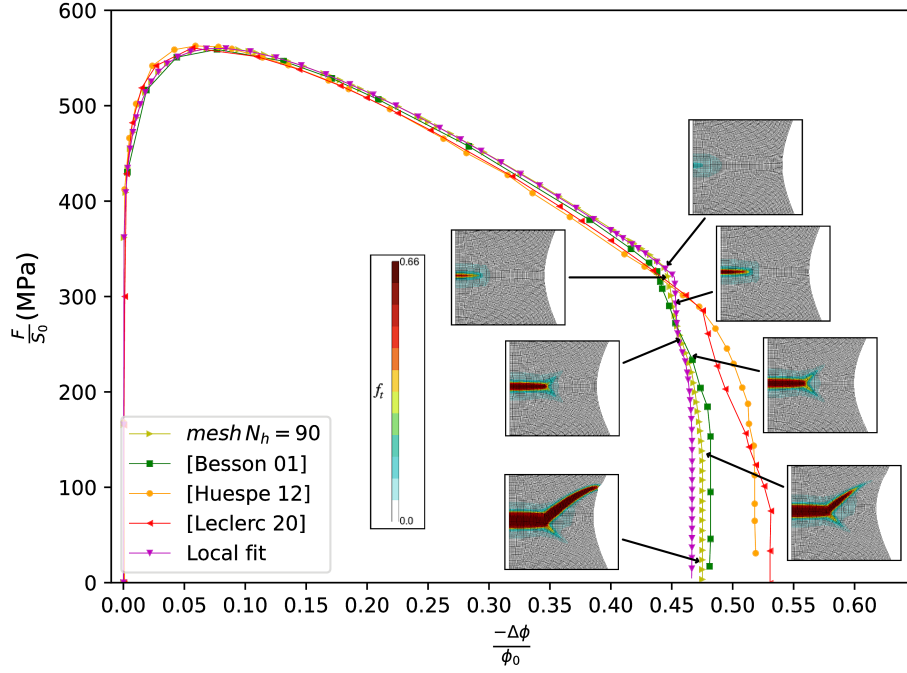


Figure 3: Evolution, for the nonlocal model, of the engineering stress as a function of the diameter reduction $-\Delta\phi/\phi_0$ for the axisymmetric specimen with a central spatial discretization of $N_h = 90$. The confrontation with global curves from the literature ([Besson et al., 2001](#); [Huespe et al., 2012](#); [Leclerc et al., 2020](#)) and the local model indicates a correct parameter fit. Total porosity is displayed at various times of the simulation to illustrate the formation of the expected cup-cone crack path.

In contrast, the global response for the plane strain simulation (presented in figure 4) shows a slight overestimation of the strain at crack initiation compared to the reference and a higher total failure strain. This difference can be explained by the fact that the crack path remains flat (as can be seen on the images of the total porosity maps taken at different stages of propagation). This result is not in agreement with experimental data as well as the simulation using the local framework, which both exhibit slant fracture. The effect of the characteristic lengths on the crack path is discussed below in section 6 where it is shown that slant fracture may indeed be obtained using the nonlocal framework and a proper choice for the characteristic lengths.

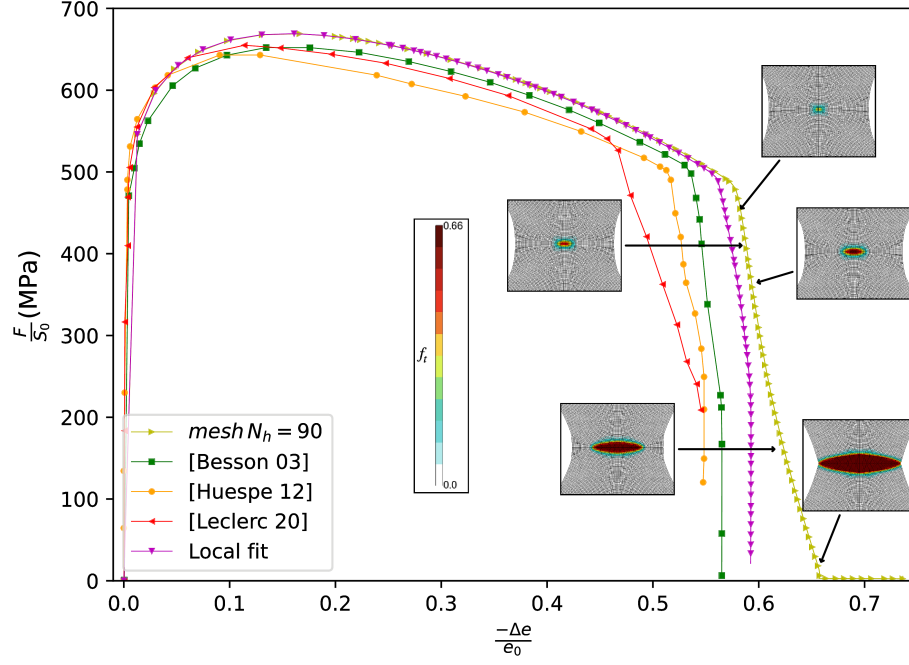


Figure 4: Evolution, for the nonlocal model, of the engineering stress as a function of the thickness reduction $-\Delta e/e_0$ for the plane strain specimen with a central spatial discretization of $N_h = 90$. The confrontation with global curves from the literature (Besson et al., 2003; Huespe et al., 2012; Leclerc et al., 2020) and the local model indicates a correct parameter fit. Total porosity is displayed at various steps of the simulation to illustrate the propagation of a flat crack instead of a slanted one. This illustrates the need to properly calibrate the nonlocal characteristic lengths.

4. Study of the convergence properties of the nonlocal model

In this section, the convergence of the solution with respect to mesh size and mesh orientation is first checked. This allows to determine the mesh size needed to obtain convergence as a function of the internal lengths, which are assumed to be equal. Using the appropriate mesh size, it is then possible to establish a relation between the internal lengths and the numerically obtained band widths.

4.1. Effect of mesh size

Several meshes with the same element initial aspect ratio $r_h = 6$ and the same orientation, but different element sizes are used to study the effect of mesh size.

Local model. In the case of the local model, the considered set of number of elements in the width of the central section N_h is: 45, 60, 75 or 90. The

engineering stress (F/S_0) is plotted as a function of the variation of the minimum diameter $-\Delta\phi/\phi_0$ for different mesh sizes in figure 5. On the same graph, the distribution of total porosity f at total failure is shown for the different meshes. Let us note that all the simulations predict crack initiation for the same diameter reduction and that the diameters at full failure ($F/S_0 = 0$) only slightly differ. In this particular case, the well-known mesh size dependency (see *e.g.* (Liu et al., 1994; Rousselier et al., 1989)) has no significant effect on the global response as the load drop is very sharp. Indeed, whatever the mesh size, the highly damaged area is localized within one row of elements.

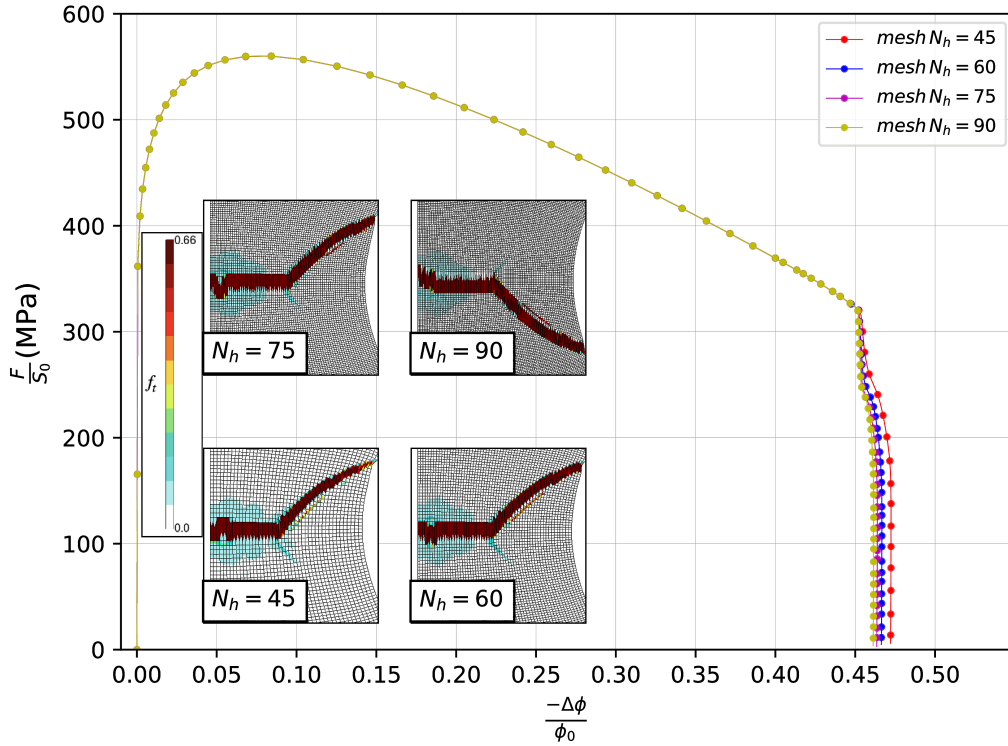


Figure 5: Evolution, for the local model, of the engineering stress as a function of the diameter reduction $-\Delta\phi/\phi_0$ for different spatial discretization in the case of the axisymmetric specimen. The similarity of the global responses does not enable to observe a dependence on the mesh size. The total porosity for each mesh size at total failure shows a cup-cone failure with a slight deviation near the axis of symmetry.

Nonlocal model. In the case of the nonlocal model, the considered set of the number of elements in the width of the central section N_h is: 20, 45, 60, 75, 90, or

180. In figure 6, the engineering stress—diameter reduction curves and the total porosity f at total failure are shown for the different meshes. The global response appears to be converged, and the simulation leads to a cup cone crack path as soon as $N_h \geq 45$. Let us note that, for the coarsest mesh ($N_h = 20$), the global response is very different than for the other meshes close to full failure. In that case, there is no crack bifurcation so that the minimum diameter always plastically deforms. In the case of cup–cone failure, the material undergoes elastic unloading at the notch root due to crack bifurcation at some stage of loading so that the minimum diameter no longer changes. Obviously, for $N_h = 20$, the mesh is too coarse to properly capture the width of the highly damaged zone, and the simulation is, in that case, mesh size-dependent. In all cases where cup–cone fracture is obtained, there exist two possible symmetric crack paths when flat propagation ends. One path is selected, but the other path can still be visualized. In the case of the smallest mesh size ($N_h = 180$) a zigzagging crack path is obtained. In that case, the crack first runs downwards (-45°) and then upwards ($+45^\circ$). Such a behavior is often experimentally observed (Besson et al., 2001).

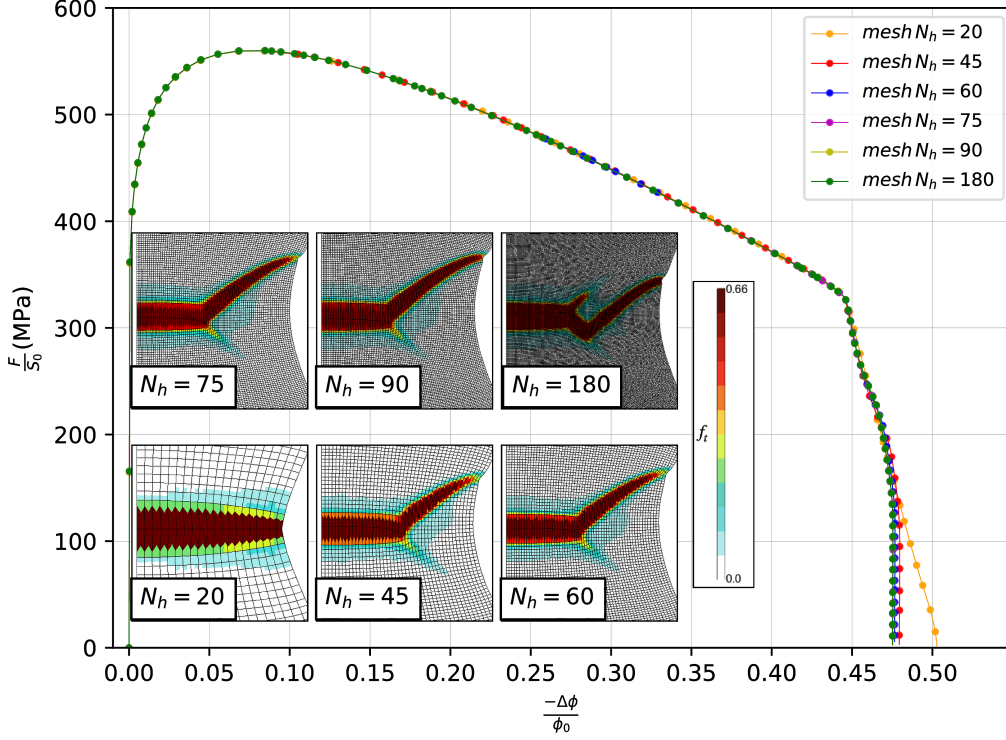


Figure 6: Evolution, for the nonlocal model, of the engineering stress as a function of the diameter reduction $-\Delta\phi/\phi_0$ for different spatial discretization in the case of the axisymmetric specimen. The global responses are similar for the mesh sizes $N_h > 20$. The total porosity for each mesh size at total failure shows a cup-cone failure with a straight first horizontal part except for the coarsest mesh size $N_h = 20$, which exhibits a flat crack path. The finest mesh size $N_h = 180$ enables the crack path to bifurcate twice, which can also be experimentally observed. These results indicate mesh independence.

4.2. Effect of mesh orientation

In this section, three meshes having the same number of elements in the central part and the same initial ratio $r_h = 6 : 1$ are used. However, the mesh is slightly tilted with respect to the horizontal axis. The tilt angles are: 0° , 5° and 10° . Note that because of large strain, the final tilt angle is much larger than the initial one.

Local model. In the case of the local model, the number of elements in the central part is $N_h = 60$. In figure 7, the global responses and the total porosity f at total failure are shown for the different meshes. Although the global responses are very similar, it is interesting to note that each mesh leads to a different crack

path. Indeed, when there is no tilt, a classical cup–cone fracture path is obtained, as shown above. For a tilt angle of 5° , the crack first runs upwards from the center of the specimen and then runs downwards after reaching the mid-radius. For a tilt angle of 10° , the crack runs upwards following one row of elements. In both cases, cup–cone fracture is not observed, and the predicted crack path is only formed by cones. The local model thus clearly suffers from a strong dependence on mesh orientation. This implies that the crack path can hardly be predicted using local models. They can be useful if the predicted crack path corresponds to the expected one. In that case, the local stress and strain history can be investigated to analyze/understand crack formation. This can be done by prescribing the crack path using the computational cell methodology (Xia and Shih, 1995; Besson et al., 2013). The result also indicates that automatic meshing can hardly be used to generate the mesh because its design cannot be fully controlled. Simulations with automatic remeshing during the calculation are also not possible.

Nonlocal model. In the case of the nonlocal model, the number of elements in the central part is $N_h = 90$. This number of elements was chosen so as to approximately obtain the same band width as in the case of the local model ($N_h = 60$) following the discussion in section 3.4. Note, however, that results obtained with the local model for $N_h = 90$ also lead to the disappearance of cup-cone fracture for a tilt angle equal to 5 and 10° . In figure 8, the engineering stress–diameter reduction curves and the total porosity f at total failure are shown for the different meshes. All the simulations give the same global response and lead to a similar cup–cone crack path. In all cases, the band width of the damage localization band is the same. Therefore, it can be concluded that results are converged and insensitive to mesh orientation. This paves the way for the use of automatic meshing techniques of complex parts and remeshing.

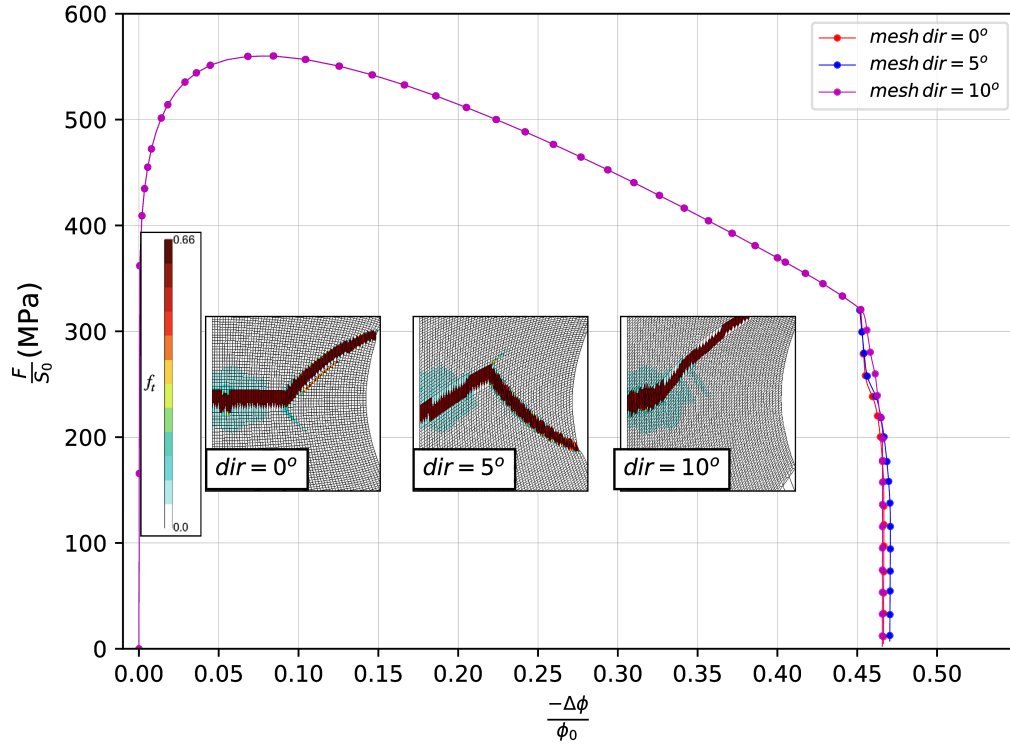


Figure 7: Evolution, for the local model, of the engineering stress as a function of the diameter reduction $-\Delta\phi/\phi_0$ for various mesh orientations in the case of the axisymmetric specimen. The global responses are similar for all the orientations. However, the total porosity for each mesh size at total failure shows a different crack path for each mesh orientation, which indicates mesh dependence.

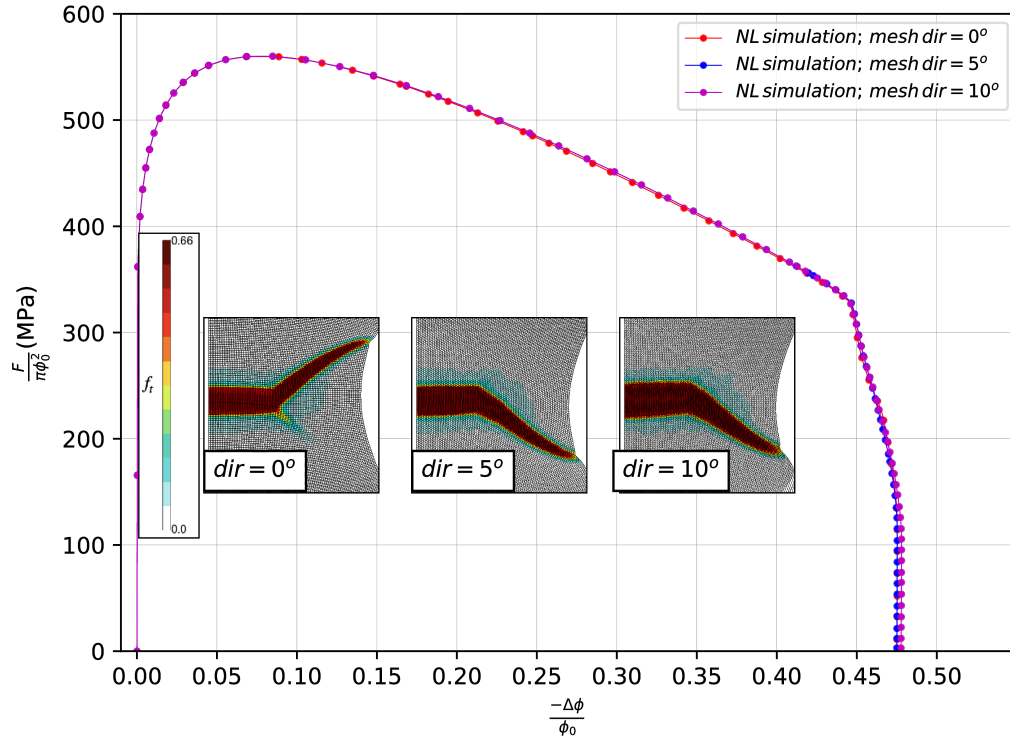


Figure 8: Evolution, for the nonlocal model, of the engineering stress as a function of the diameter reduction $-\Delta\phi/\phi_0$ for various mesh orientations in the case of the axisymmetric specimen. The global responses are similar for all orientations. Besides, the total porosity for each mesh size at total failure shows an identical cup-cone crack path for each mesh orientation. These observations indicate mesh independence.

5. Analysis of the damage localization bands

In this section, the relation between the characteristic length and the width of the localization band is investigated. To do so, it is first necessary to define how to measure the width of a localization band. The finite element discretization needed to obtain a converged band width is then investigated. Based on these results, the relation between the characteristic length and the band width is studied for both axisymmetric and plane strain specimens, as this relationship may depend on the stress state.

5.1. Definition of the band width

In the literature, there is no agreement, to the authors' knowledge, on a definition of a measure of the width of the localization bands. [Maziere et al. \(2010\)](#) study localized bands in a nickel-based superalloy which exhibits a Portevin–Le Chatelier effect. Their proposed method is based on the analysis of the local plastic strain rate. It is applied to FE simulations but is designed to mimic actual experimental techniques (see references in the paper). In [\(Labergere et al., 2014\)](#), the authors study a copper sheet and also use the strain rate profile to determine the band width. The profile is fitted by a pseudo-Voigt function for which the band width is a fitting parameter. [Gorodetskyi et al. \(2017\)](#) propose a method able to detect discontinuities such as displacement jumps which can be applied to both FE simulations and experimental DIC results. In [\(Ait-Amokhtar et al., 2006\)](#), plastic strain localization is experimentally studied as a function of the applied strain rate in the case of an Al–Mg alloy exhibiting a PLC effect. The bandwidth is defined “as the width at the middle height of the localized strain band”. In this study, it is proposed to define the band width (referred to as l_b^v for variable $v = \bar{\omega}$ or $v = \bar{\kappa}$) as the width over which the considered variable reaches half its maximum value. In that sense, this definition corresponds to that of [Ait-Amokhtar et al. \(2006\)](#). In the following, the case of the axisymmetric specimen will only be described as similar results are obtained for the plane strain specimen. Profiles in the deformed configuration along the symmetry axis for both $\bar{\omega}$ and ω are exemplified in [fig. 9](#) where the band width for $\bar{\omega}$ is shown by the blue arrows and the band width for ω by the red arrows. The profiles for $\bar{\omega}$ can easily be plotted as this variable is defined at nodes and can be interpolated. Plotting the profiles for the local variable ω first requires extrapolating values at Gauss points to nodes (red curve in [figure 9](#)). In all cases, the band width for the local variable is about the size of one single element in the deformed configuration. In the following, the width of the localization bands is determined when the maximum of $\bar{\omega}$ reaches 0.5 along the profile. In

that case, the material points are close to full failure. Applying this definition to measure the band width for the local and nonlocal volume variations along the vertical symmetry axis for the axisymmetric specimen leads to consistent relative measures. Indeed, as shown in fig. 9, the band width measured on $\bar{\omega}$ is larger than the band width measured on its local counterpart ω , even if the maximum of the nonlocal variable is lower than the maximum of the local variable, as expected using an implicit gradient nonlocal formulation.

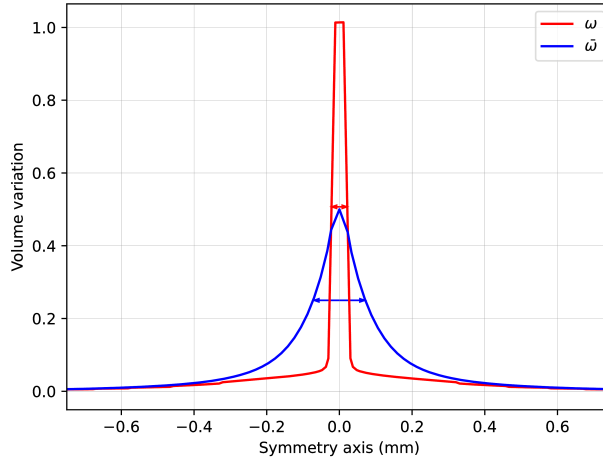


Figure 9: Band width measure for the nonlocal volume variation $\bar{\omega}$ when $\bar{\omega}_{\max} = 0.5$. Evolution of the local and nonlocal volume variations along the symmetry axis. The double arrows show the measure of the corresponding band widths l_b^ω and $l_b^{\bar{\omega}}$.

5.2. Conditions to obtain a converged band width

In this part, the evolution of the band width with element size is studied. As the present model makes use of gradients of $\bar{\omega}$ and $\bar{\kappa}$ computed in the current configuration, it is important to evaluate the localization band width in the deformed configuration as proposed above. The element height after deformation and when fracture starts is referred to as H_{r1} in the following (see fig. 10). The element height along the element row just above is referred to as H_{r2} . Due to different loading histories, the element elongation at fracture can differ greatly from one simulation to another. It is therefore important that the initial element height (h_{\min}) is small enough to assure that the element height at fracture (H_{r1}) is still able to represent the localization band. The convergence of the band width should therefore be checked with respect to H_{r1} .

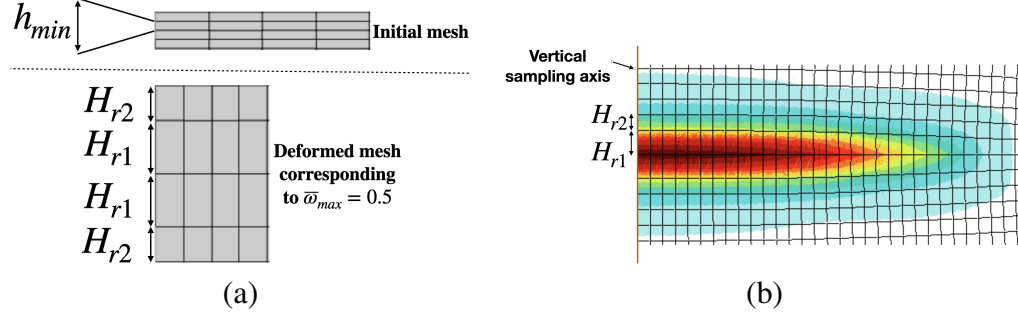


Figure 10: (a) Definition of H_{r1} and H_{r2} . (b) Contours of the nonlocal volume variation $\bar{\omega}$ when $\bar{\omega}_{max} = 0.5$. Arrows here define current element heights H_{r1} and H_{r2} .

Different values for the number of element along the thickness of the specimens are used: $N_h = 540, 270, 180, 90, 60, 45, 30, 20$. This study is performed for two values of the characteristic length, taken here equal for both nonlocal variables ($l_\kappa = l_\omega = 80\mu\text{m}$ and $l_\kappa = l_\omega = 40\mu\text{m}$). Both axisymmetric and plane strain specimens are considered. The considered variable is the nonlocal volume variation but similar results can be obtained if the nonlocal effective accumulated plastic strain is used to measure the localization band width.

Figure 11 shows the evolution of the band width size as a function of the element height in the current configuration (H_{r1}), as defined in fig. 10. Each set of points can be approximated by a line, which means that it can be assumed that the band width is an affine function of the mesh size. Using this approximation, the band width for $H_{r1} \rightarrow 0$ can be extrapolated to a non-zero value which is an estimated value of the band width l_b^∞ free from discretization error. In practical applications, this error is always present.

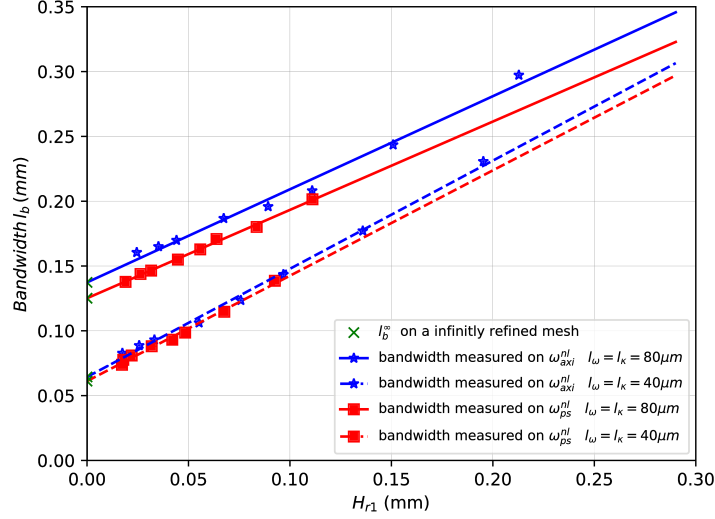


Figure 11: Evolution of the measured band width for both $l_\kappa = l_\omega = 40\mu m$ and $l_\kappa = l_\omega = 80\mu m$ on both the axisymmetric and plane strain tensile tests as a function of the element height in the current configuration H_{r1} . There appears to be a linear relation between the band width and the element height. This means that it is possible to estimate a value of the band width l_b^∞ free from any discretization error for $H_{r1} = 0$.

5.3. Relation between the band width and the internal lengths l_κ and l_ω

Let us note that in fig. 11, for a given geometry, the line corresponding to the largest characteristic length (*i.e.* $l_\kappa = l_\omega = 80\mu m$) has approximately the same slope as the line corresponding to a smallest characteristic length (*i.e.* $l_\kappa = l_\omega = 40\mu m$) but leads to a higher band width estimate l_b^∞ . In order to validate this observation for other characteristic lengths and to establish a simple relation between the characteristic length and the band width l_b^∞ , the same series of simulations was performed for additional values for of $l_\omega = l_\kappa$: *i.e.* $20\mu m$, $60\mu m$, and $100\mu m$. Plotting the evolution of the measured band width l_b^∞ versus the imposed characteristic length (see fig. 12), it can be observed that for a given geometry, the measured points approximately lie on a line. Using this regression, it is observed, as expected, that a null band width is obtained when the characteristic length is also null. Let us note that the slope in this linear relationship is different for each geometry. However, the difference between the relation obtained for plane strain and axisymmetric elements remains small: $l_b^\infty \approx 1.54l_{\kappa,\omega}$ in the first case and $l_b^\infty \approx 1.69l_{\kappa,\omega}$ in the second case. This simple relation presents a major advantage as it enables to estimate, for a given geometry, and based on the choice of the characteristic length, the width of the localization

band. It is then possible to choose the number and size of the elements in the localization band (respectively denoted a and H_{r1}) in order to properly capture its gradients with: $a \times H_{r1} < l_b^\infty$. In all the nonlocal simulations of this paper (except for fig. 6), the factor a is at least equal to 3, *i.e.* there are at least three P2P1P1 elements in the band width at the onset of failure.

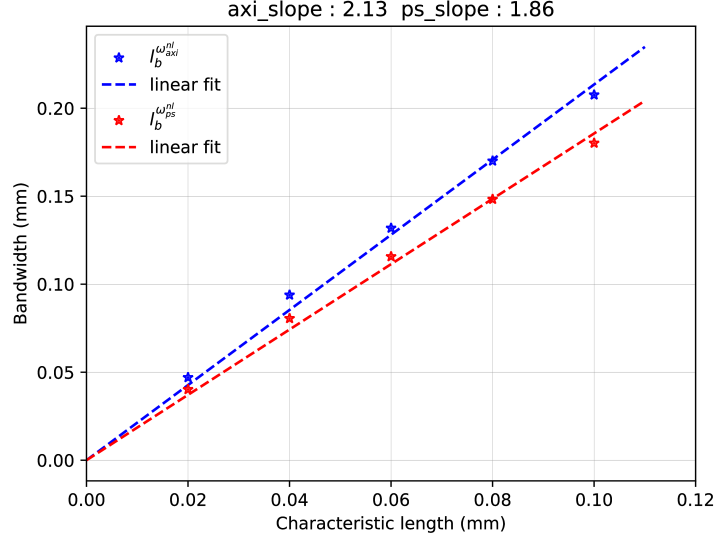


Figure 12: Evolution of the estimated band width free from discretization error for both the axisymmetric and plane strain tensile tests as a function of the characteristic length ($l_\kappa = l_\omega$). There appears to be a proportional relation between the band width and the characteristic length, with slightly different coefficients for each geometry. This means that it is possible to estimate the size the band width for a given characteristic length and a given geometry.

6. Using two characteristic lengths to model the cup–cone and slant fracture

In this section, two different characteristic lengths ($l_\kappa \leq l_\omega$) are used to model the occurrence of cup–cone and slant fracture.

6.1. Procedure

Several simulations were performed for different characteristic lengths varying between $20\mu\text{m}$ and $100\mu\text{m}$ and different ratios l_ω/l_κ (*i.e.* 1, 2, 3, 4 and 5). Let us note that larger ratios were not considered in order to avoid too large computational costs due to mesh refinement associated with the requirement to have 3 elements in the band width at the onset of fracture ($3 \times H_{r1} < l_b^\infty$).

The relative values of the two characteristic lengths are chosen to be consistent with the physical degradation of metallic materials, and especially steels. Indeed, in steels, two damage mechanisms exist: (i) void growth from sulfides/oxides and (ii) damage nucleation at iron carbides Fe_3C , which occurs at high strains (Tanguy et al., 2008). As the spacing between sulfides/oxides is larger than between carbides, it makes sense to only consider $l_\omega \geq l_\kappa$.

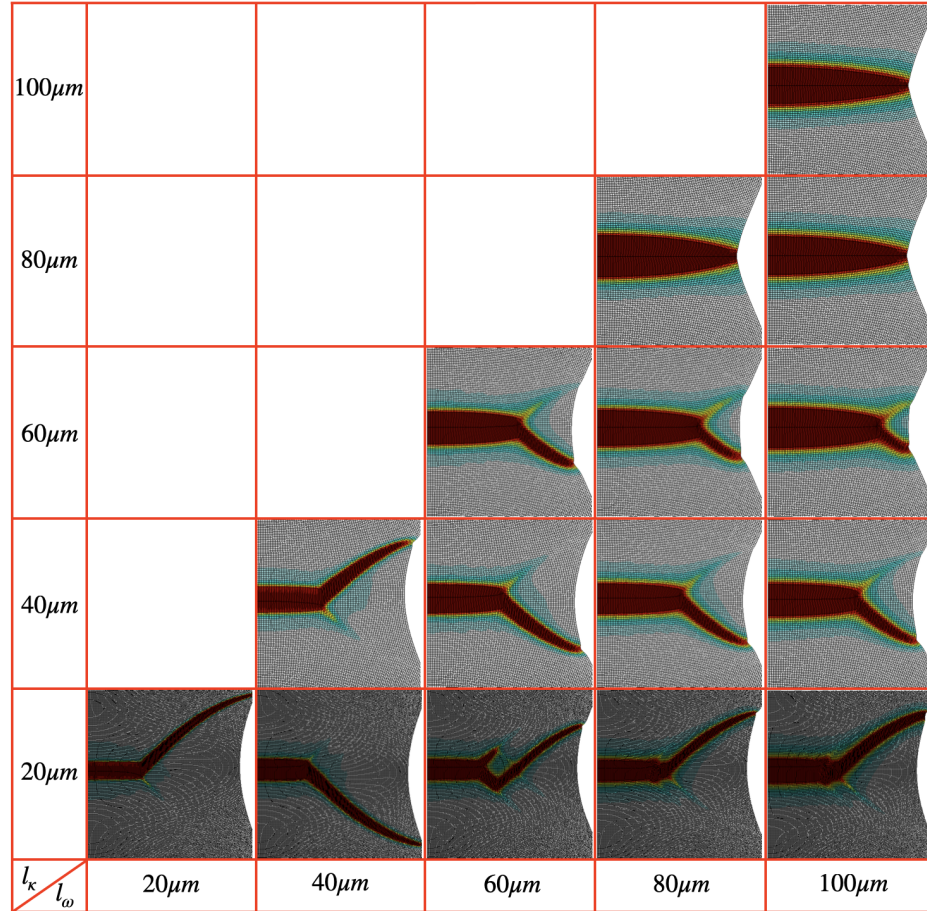


Figure 13: Contours of total porosity at total fracture for different characteristic lengths l_κ and l_ω for the axisymmetric specimen. Cup-cone crack paths are observed only for $l_\kappa < 80\mu m$. The characteristic length l_κ should then be relatively small compared to the specimen size to observe a cup-cone fracture. The larger the characteristic lengths, the wider the localization band (which is linked to the displacement at failure) and the further from the symmetry axis the bifurcation..

6.2. Cup–cone fracture

For the axisymmetric specimen, the contours of total porosity at full fracture for different characteristic lengths are displayed in fig. 13. It appears that large values for l_κ prevent the occurrence of crack bifurcation for the considered specimen. As seen in fig. 13, simulations with $l_\kappa \geq 80\mu\text{m}$ predict a flat crack while all simulations with $l_\kappa < 80\mu\text{m}$ predict the cup–cone crack path. For a given value of l_κ , it can be noticed that the larger l_ω , the wider the localization band. Similarly, for a given value of l_ω , the band width increases with increasing l_κ . This is indeed expected since a large characteristic length leads to a larger band. In addition larger bands tend to increase the length of the flat part of the crack path. The flat central crack then bifurcates to form the slanted crack path at $+45^\circ$ or -45° . In one case ($l_\omega = 60\mu\text{m}$ and $l_\kappa = 20\mu\text{m}$) a zigzagging crack path is obtained, but it was impossible to determine why such a crack path was formed, although this phenomenon is often experimentally observed.

6.3. Slant fracture

For the plane strain specimen, the contours of total porosity at total fracture for different characteristic lengths are displayed in fig. 14. For $l_\kappa \geq 40\mu\text{m}$ flat fracture is always obtained so that only one crack path is shown ($l_\omega = l_\kappa = 40\mu\text{m}$). For $l_\kappa = 20\mu\text{m}$ slant fracture is always obtained (V–shape). In that case, the effect of l_ω is small. The band width only slightly increases with increasing l_ω .

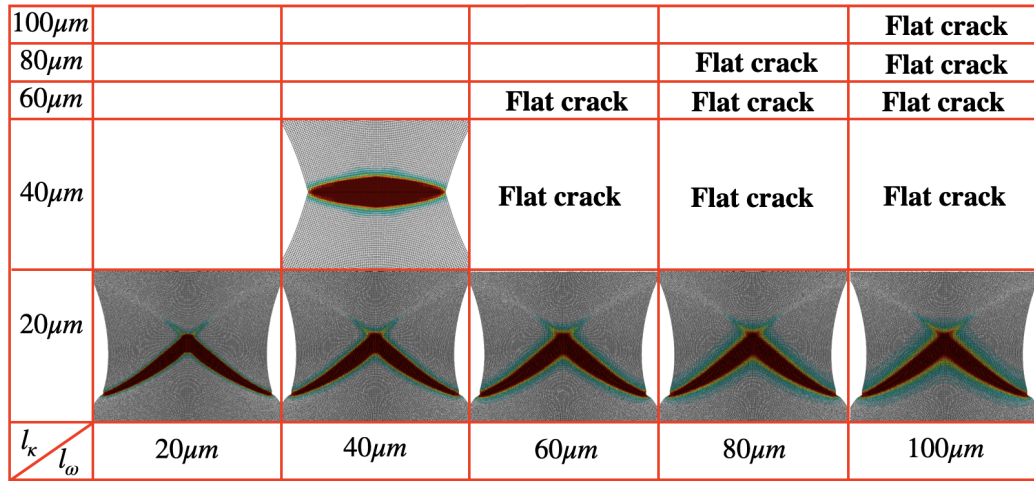


Figure 14: Contours of total porosity at total fracture for different characteristic lengths l_κ and l_ω for the plane strain case. Slant fracture is observed only for $l_\kappa = 20\mu\text{m}$. The effect of l_ω appears to be limited in this case.

6.4. Size effect

It is interesting to revisit the above observations from a more physical point of view and to consider, for a given set of material lengths, how specimen size impacts the formation of the cup–cone and slant fracture. Indeed increasing the material lengths for a given specimen size is equivalent to decreasing the size of the specimen for given material lengths. Similar crack paths are obtained as long as the ratios l_ω/L and l_κ/L are constant where L is a characteristic dimension of the simulated structure (diameter or thickness in the present case).

From the results corresponding to the axisymmetric specimen (fig. 13), it can be concluded that it is easier to form a cup–cone crack path for large specimens (case corresponding to $l_\kappa < 80\mu\text{m}$ for a given geometry) than for smaller specimen sizes. From the results corresponding to the plane strain specimen (fig. 14), it can be concluded that only sufficiently large plane strain specimens break following the slant crack path. This opens the way to the determination of material lengths by using homothetic specimens so as to obtain different crack paths. Lengths could be fitted to represent the different fracture patterns. This will obviously require the use of very small specimens in the case of metals where lengths are expected to be of the order of the mean spacing between damage initiation sites.

7. Conclusions

In this work, a nonlocal GTN model for ductile fracture was proposed which uses two material lengths. The model is based on an implicit gradient formulation applied to the plastic volume variation (material length l_ω) and the accumulated plastic strain (material length l_κ). The model allows to regularize void growth and strain-controlled nucleation. The model parameters are fitted to reproduce the global response for tests carried out on a pipe line steel using a tensile bar and a plane strain specimen. These experiments have already been used in the literature to test several models and numerical techniques. Each test is representative of a characteristic crack path: cup–cone fracture (tensile test) and slant fracture (plane strain test).

The material parameters were first fitted assuming that both lengths are equal ($l_\omega = l_\kappa$) in order to reproduce the macroscopic behavior of both specimens. It was checked that mesh independence is obtained if a sufficiently fine mesh is used. In particular, it was shown that a local model is strongly dependent on mesh design (mesh orientation in the present study) whereas the nonlocal model is not. This implies that remeshing cannot be applied if a local model is used but with a

nonlocal model, it can be a solution to reduce computational cost in cases where long crack propagation needs to be simulated.

A novel methodology was proposed to estimate, for a given geometry, the band width associated with a given characteristic length free from discretization error. By applying this methodology for different characteristic lengths, it was possible to establish a linear relation between the estimated band width and the characteristic length. This piece of information was then used to select the proper discretization of the localization bands for given values of the characteristic lengths in order to obtain converged solutions. In practice, the element size at failure is recommended to be three times smaller than the characteristic lengths.

Finally, two distinct characteristic lengths were used to simulate both test cases. It was first concluded that the characteristic length controlling strain controlled damage nucleation plays an important role on the occurrence of crack bifurcation: it must be small enough relative to the specimen size in order to observe a cup–cone crack path or a slanted crack path. It was also noted that increasing the characteristic lengths leads to an increase of both the band width and the radius at which the cup–cone crack path starts to bifurcate and propagate either at $+45^\circ$ or -45° . Larger values favor flat crack advance. This study also enabled to conclude that crack path should be affected by the size of the specimens. Pure flat fracture should be favored when using (very) small specimens. It could theoretically be possible to identify them separately. This paves the way for the more direct determination of material lengths by using homothetic specimens to obtain different crack paths. The fitted lengths should then be able to represent both the macroscopic behavior and the crack path for all sample sizes.

Appendix A. Implementation of the nonlocal GTN model

Integrating the set of equations 16 to 20 over a finite time step Δt using a fully implicit scheme is equivalent to solving the following set of non linear equations with respect to the increments of the state variables $\Delta \mathbf{V}_S = (\Delta \epsilon_e, \Delta \kappa, \Delta f_g, \Delta f_n, \Delta \omega)$ for a given increment of the input variables $\Delta \mathbf{V}_{IN} =$

$(\Delta\boldsymbol{\varepsilon}, \Delta\bar{\omega}, \Delta\bar{\kappa}) :$

$$\mathbf{R}_e = \Delta\boldsymbol{\varepsilon}_e + (1-f)\Delta\kappa\mathbf{n} - \Delta\boldsymbol{\varepsilon} \quad (\text{A.1})$$

$$R_\kappa = \Delta\kappa - \mathcal{F}(\Phi)\Delta t \quad (\text{A.2})$$

$$R_g = \Delta f_g - (1-f)\Delta\bar{\omega} \quad (\text{A.3})$$

$$R_n = \Delta f_n - A_n\Delta\bar{\kappa} \quad (\text{A.4})$$

$$R_\omega = \Delta\omega - (1-f)\Delta\kappa\text{trace}(\mathbf{n}) \quad (\text{A.5})$$

Using a fully implicit scheme, all variables in the previous system are evaluated at the end of the time increment. Solving the system requires the evaluation of its Jacobian matrix which is formally expressed as:

$$\mathbf{J} = \frac{\partial \mathbf{R}}{\partial \Delta \mathbf{V}_s} \quad (\text{A.6})$$

where $\mathbf{R} = (\mathbf{R}_e, R_\kappa, R_g, R_n, R_\omega)$. The Jacobian matrix can be computed block-wise as follows (the zero terms are omitted).

• Derivatives of \mathbf{R}_e :

$$\frac{\partial \mathbf{R}_e}{\partial \Delta \boldsymbol{\varepsilon}_e} = \mathbb{I} + (1-f)\Delta\kappa\mathbb{N} : \mathbb{E} \quad \text{with } \mathbb{N} = \frac{\partial \mathbf{n}}{\partial \boldsymbol{\sigma}} \quad (\text{A.7})$$

$$\frac{\partial \mathbf{R}_e}{\partial \Delta \kappa} = (1-f)\mathbf{n} \quad (\text{A.8})$$

$$\frac{\partial \mathbf{R}_e}{\partial \Delta f_g} = (1-f)\Delta\kappa\mathbf{n}_f - \Delta\kappa\mathbf{n} \quad \text{with } \mathbf{n}_f = \frac{\partial \mathbf{n}}{\partial f} \quad (\text{A.9})$$

$$\frac{\partial \mathbf{R}_e}{\partial \Delta f_n} = (1-f)\Delta\kappa\mathbf{n}_f - \Delta\kappa\mathbf{n} \quad (\text{A.10})$$

• Derivatives of R_κ :

$$\frac{\partial R_\kappa}{\partial \Delta \boldsymbol{\varepsilon}_e} = -(\mathcal{F}'\Delta t)\mathbf{n} : \mathbb{E} \quad \text{with } \mathcal{F}' = d\mathcal{F}/d\Phi \quad (\text{A.11})$$

$$\frac{\partial R_\kappa}{\partial \Delta \kappa} = 1 - \mathcal{F}'H\Delta t \quad \text{with } H = dR/d\kappa \quad (\text{A.12})$$

$$\frac{\partial R_\kappa}{\partial \Delta f_g} = -\mathcal{F}'\sigma_{*f}\Delta t \quad \text{with } \sigma_{*f} = \frac{\partial \sigma_*}{\partial f} \quad (\text{A.13})$$

$$\frac{\partial R_\kappa}{\partial \Delta f_n} = -\mathcal{F}'\sigma_{*f}\Delta t \quad (\text{A.14})$$

- Derivatives of R_g :

$$\frac{\partial R_g}{\partial \Delta f_g} = 1 + \Delta \bar{\omega} \quad (\text{A.15})$$

$$\frac{\partial R_g}{\partial \Delta f_n} = \Delta \bar{\omega} \quad (\text{A.16})$$

- Derivatives of R_n :

$$\frac{\partial R_n}{\partial \Delta f_n} = 1 \quad (\text{A.17})$$

- Derivatives of R_ω :

$$\frac{\partial R_\omega}{\partial \Delta \epsilon_e} = -(1-f) \Delta \kappa \mathbf{I} : \mathbb{N} : \mathbb{E} \quad (\text{A.18})$$

$$\frac{\partial R_\omega}{\partial \Delta \kappa} = -(1-f) \text{trace}(\mathbf{n}) \quad (\text{A.19})$$

$$\frac{\partial R_\omega}{\partial \Delta f_g} = -(1-f) \Delta \kappa \text{trace}(\mathbf{n}_f) \quad (\text{A.20})$$

$$\frac{\partial R_\omega}{\partial \Delta f_n} = -(1-f) \Delta \kappa \text{trace}(\mathbf{n}_f) \quad (\text{A.21})$$

$$\frac{\partial R_\omega}{\partial \Delta \omega} = 1 \quad (\text{A.22})$$

The partial derivatives of σ_\star are obtained considering the stationarity of the G function (eq. 3) : $G = 0$ and $\delta G = 0$. One then has:

$$\chi = \frac{1}{h} = \frac{\partial G}{\partial \sigma_\star}, \quad \mathbf{n} = \frac{\partial \sigma_\star}{\partial \boldsymbol{\sigma}} = -h \frac{\partial G}{\partial \boldsymbol{\sigma}} = -h \boldsymbol{\nu}, \quad \frac{\partial \sigma_\star}{\partial f} = -h \frac{\partial G}{\partial f}, \quad (\text{A.23})$$

and

$$\mathbb{N} = \frac{\partial \mathbf{n}}{\partial \boldsymbol{\sigma}} = -h \frac{\partial^2 G}{\partial \boldsymbol{\sigma}^2} - h^3 \frac{\partial^2 G}{\partial \sigma_\star^2} \boldsymbol{\nu} \otimes \boldsymbol{\nu} + h^2 \left(\frac{\partial^2 G}{\partial \boldsymbol{\sigma} \partial \sigma_\star} \otimes \boldsymbol{\nu} + \boldsymbol{\nu} \otimes \frac{\partial^2 G}{\partial \boldsymbol{\sigma} \partial \sigma_\star} \right) \quad (\text{A.24})$$

and

$$\mathbf{n}_f = \frac{\partial \mathbf{n}}{\partial f} = -h \frac{\partial^2 G}{\partial \boldsymbol{\sigma} \partial f} + h^2 \frac{\partial G}{\partial f} \frac{\partial^2 G}{\partial \boldsymbol{\sigma} \partial \sigma_\star} + h^2 \left(\frac{\partial^2 G}{\partial \sigma_\star \partial f} - h \frac{\partial^2 G}{\partial \sigma_\star^2} \frac{\partial G}{\partial f} \right) \boldsymbol{\nu} \quad (\text{A.25})$$

Appendix B. Consistent tangent matrix

Once the solution of the system of equations A.1 to A.5 is found, it becomes possible to numerically compute the consistent tangent matrix. For any given small variation of the input variables $\delta \mathbf{V}_{\text{IN}}$, the state variables will be modified so that \mathbf{R} remains null. One therefore has:

$$\delta \mathbf{T} = \delta \mathbf{0} = \frac{\partial \mathbf{R}}{\partial \Delta \mathbf{V}_{\text{IN}}} \cdot \delta \mathbf{V}_{\text{IN}} + \frac{\partial \mathbf{R}}{\partial \Delta \mathbf{V}_{\text{S}}} \cdot \delta \mathbf{V}_{\text{S}} = \frac{\partial \mathbf{R}}{\partial \Delta \mathbf{V}_{\text{IN}}} \cdot \delta \mathbf{V}_{\text{IN}} + \mathbf{J} \cdot \delta \mathbf{V}_{\text{S}} \quad (\text{B.1})$$

so that

$$\delta \mathbf{V}_{\text{S}} = -\mathbf{J}^{-1} \cdot \frac{\partial \mathbf{R}}{\partial \Delta \mathbf{V}_{\text{IN}}} \cdot \delta \mathbf{V}_{\text{IN}} \quad (\text{B.2})$$

The outputs variable are expressed as function of the state variables only so that:

$$\delta \mathbf{V}_{\text{OUT}} = \frac{\partial \Delta \mathbf{V}_{\text{OUT}}}{\partial \Delta \mathbf{V}_{\text{S}}} \cdot \delta \mathbf{V}_{\text{S}} = -\frac{\partial \Delta \mathbf{V}_{\text{OUT}}}{\partial \Delta \mathbf{V}_{\text{S}}} \cdot \mathbf{J}^{-1} \cdot \frac{\partial \mathbf{R}}{\partial \Delta \mathbf{V}_{\text{IN}}} \cdot \delta \mathbf{V}_{\text{IN}} \quad (\text{B.3})$$

so that the consistent tangent matrix is equal to:

$$\mathbf{K}^{\text{mat}} = -\frac{\partial \Delta \mathbf{V}_{\text{OUT}}}{\partial \Delta \mathbf{V}_{\text{S}}} \cdot \mathbf{J}^{-1} \cdot \frac{\partial \mathbf{R}}{\partial \Delta \mathbf{V}_{\text{IN}}} = \begin{pmatrix} \frac{\partial \Delta \sigma}{\partial \Delta \epsilon} & \frac{\partial \Delta \sigma}{\partial \Delta \bar{\omega}} & \frac{\partial \Delta \sigma}{\partial \Delta \bar{\kappa}} \\ \frac{\partial \Delta \omega}{\partial \Delta \epsilon} & \frac{\partial \Delta \omega}{\partial \Delta \bar{\omega}} & \frac{\partial \Delta \omega}{\partial \Delta \bar{\kappa}} \\ \frac{\partial \Delta \kappa}{\partial \Delta \epsilon} & \frac{\partial \Delta \kappa}{\partial \Delta \bar{\omega}} & \frac{\partial \Delta \kappa}{\partial \Delta \bar{\kappa}} \end{pmatrix} \quad (\text{B.4})$$

The matrices $\partial \mathbf{R} / \partial \Delta \mathbf{V}_{\text{IN}}$ and $\partial \Delta \mathbf{V}_{\text{OUT}} / \partial \Delta \mathbf{V}_{\text{S}}$ are computed as block-matrices. The calculation is straightforward with:

$$\frac{\partial \mathbf{R}_e}{\partial \Delta \epsilon} = -\mathbb{I}, \quad \frac{\partial \mathbf{R}_g}{\partial \Delta \bar{\omega}} = -(1 - f), \quad \frac{\partial \mathbf{R}_n}{\partial \Delta \bar{\kappa}} = -A_n \quad (\text{B.5})$$

and

$$\frac{\partial \Delta \sigma}{\partial \Delta \epsilon_e} = \mathbb{E}, \quad \frac{\partial \Delta \kappa}{\partial \Delta \kappa} = 1, \quad \frac{\partial \Delta \omega}{\partial \Delta \omega} = 1 \quad (\text{B.6})$$

Indeed, in the case of κ and ω , the output and state variables are similar. All other terms are null.

Appendix C. Global problem discretization

Appendix C.1. Spatial discretization

Elements have nodal DOFs corresponding to the displacements and nonlocal variables $\bar{\kappa}$ and $\bar{\omega}$. They are represented as vector \mathbf{u}^e , $\bar{\kappa}^e$ and $\bar{\omega}^e$. Linear shape functions are used to interpolate the nonlocal nodal variables in the elements (i.e. $\bar{\kappa}^e$ and $\bar{\omega}^e$), so that:

$$\bar{\kappa} = \mathbf{N} \cdot \bar{\kappa}^e \quad \text{and} \quad \bar{\omega} = \mathbf{N} \cdot \bar{\omega}^e \quad (\text{C.1})$$

where \mathbf{N} is a matrix formed with the linear shape functions. The gradients of $\bar{\kappa}$ and $\bar{\omega}$ are computed as:

$$\vec{\nabla} \bar{\kappa} = \mathbf{G} \cdot \bar{\kappa}^e \quad \text{and} \quad \vec{\nabla} \bar{\omega} = \mathbf{G} \cdot \bar{\omega}^e \quad (\text{C.2})$$

where the matrix \mathbf{G} is formed with the derivatives of the linear shape functions with respect to the final configuration. The gradient with respect to the initial configuration is computed as $\vec{\nabla}_0 \bar{\kappa} = \mathbf{G}^0 \cdot \bar{\kappa}^e$ where \mathbf{G}^0 is formed with the derivatives of the linear shape functions with respect to the initial configuration.

Standard quadratic shape functions are used to interpolate the nodal variables associated with the displacements in the elements (i.e. \mathbf{u}^e). The transformation tensor \mathbf{F} and the velocity gradient tensor \mathbf{L} are computed as:

$$\mathbf{F} = \mathbf{1} + \mathbf{B}_F \cdot \mathbf{u}^e \quad \text{and} \quad \mathbf{L} = \mathbf{B}_L \cdot \dot{\mathbf{u}}^e \quad (\text{C.3})$$

where \mathbf{B}_F is a matrix formed with the derivatives of the quadratic shape functions with respect to the initial configuration whereas \mathbf{B}_L uses the derivatives of the same shape functions with respect to the final configuration. The deformation rate \mathbf{D} is expressed as $\mathbf{B}_D \cdot \dot{\mathbf{u}}^e$.

Appendix C.2. Temporal discretization

The finite strain formulation is obtained using a mid-point integration scheme over the time step $[t, t + \Delta t]$. The transformation tensor at $t + \frac{1}{2}\Delta t$ is first computed as $\mathbf{F}_{\frac{1}{2}} = \mathbf{R}_{\frac{1}{2}} \cdot \mathbf{U}_{\frac{1}{2}} = \mathbf{F}_1 - \frac{1}{2}\Delta \mathbf{F}$ using the standard polar decomposition. The transformation increment is then computed as:

$$\Delta \mathbf{L} = \Delta \mathbf{F} \cdot \mathbf{F}_{\frac{1}{2}}^{-1} = \Delta \mathbf{D} + \Delta \mathbf{W} \quad (\text{C.4})$$

where $\Delta \mathbf{D}$ and $\Delta \mathbf{W}$ are respectively the symmetric and skew-symmetric parts of $\Delta \mathbf{L}$. The rotation \mathbf{Q} is updated as (based on the mid-point integration of eq. 22)

$$\Delta \mathbf{Q} = \left(\mathbf{1} - \frac{1}{2}\Delta \mathbf{W} \right)^{-1} \cdot \Delta \mathbf{W} \cdot \mathbf{Q}_0 \quad (\text{C.5})$$

The strain $\Delta\epsilon$ is updated as:

$$\Delta\epsilon = Q_{\frac{1}{2}}^T \cdot \Delta D \cdot Q_{\frac{1}{2}} \quad (\text{C.6})$$

The constitutive equations are then integrated (see [Appendix A](#)) using this strain increment. The resulting stress tensor is rotated back as $\Sigma = Q_{\frac{1}{2}} \cdot \Delta\sigma \cdot Q_{\frac{1}{2}}^T$. The 2nd (e.g. $\partial\Delta\sigma/\partial\Delta\bar{\omega}$) and 4th ($\partial\Delta\sigma/\partial\Delta\epsilon$) order tensors in the consistent matrix (eq. B.4) are also rotated back using $Q_{\frac{1}{2}}$. The rotated quantities are indicated with a $^\diamond$. In particular $\partial\Delta\sigma/\partial\Delta\epsilon|^\diamond = \mathbb{C}^J$ is associated with the Jaumann rate of the stress tensor Σ . The tangent operator corresponding to the Truesdell rate is then given by:

$$\mathbb{C}^\tau = \mathbb{C}^J - \frac{1}{2}(\Sigma \otimes \underline{1} + \Sigma \otimes \bar{1} + \underline{1} \otimes \Sigma + \bar{1} \otimes \Sigma) + \Sigma \otimes \underline{1}$$

Appendix D. Details of the terms involved in the global system

Appendix D.1. Elementary reactions

From the discretized form of the weak formulation (25 and 26), elementary reactions associated unknowns are given as:

$$\mathbf{F}_\kappa = \int_{\Omega^e} (\bar{\kappa} - \kappa) \mathbf{N} + l_\kappa^2 \mathbf{G}^T \cdot \mathbf{G} \cdot \bar{\kappa}^e \, d\Omega \quad (\text{D.1})$$

$$\mathbf{F}_\omega = \int_{\Omega^e} (\bar{\omega} - \omega) \mathbf{N} + l_\omega^2 \mathbf{G}^T \cdot \mathbf{G} \cdot \bar{\omega}^e \, d\Omega \quad (\text{D.2})$$

$$\mathbf{F}_u = \int_{\Omega^e} \mathbf{B}_L^T \cdot \{\Sigma\} \, d\Omega = \int_{\Omega_0^e} \mathbf{B}_L^T \cdot \{\Sigma\} \, J d\Omega_0 \quad (\text{D.3})$$

$$(\text{D.4})$$

where notation $\{\Sigma\}$ indicates that the tensor Σ is expressed using Voigt notations. Let us underline that the integrals are taken over the *current* configuration. Integration is performed using standard Gauss integration.

Let us introduce here the function M_R such that the product c of two second order tensors a and b , usually written $c = a \cdot b$, can be expressed using Voigt notations as:

$$\{c\} = \{a \cdot b\} = M_R(b) \cdot \{a\} \quad (\text{D.5})$$

The matrix $M_R(b)$ thus depends linearly on b .

Appendix D.2. Elementary stiffness matrix

It is then necessary to evaluate the elementary stiffness matrix which is computed as a block matrix.

$$\mathbf{K} = \begin{pmatrix} \mathbf{K}_{uu} & \mathbf{K}_{u\kappa} & \mathbf{K}_{u\omega} \\ \mathbf{K}_{\kappa u} & \mathbf{K}_{\kappa\kappa} & \mathbf{K}_{\kappa\omega} \\ \mathbf{K}_{\omega u} & \mathbf{K}_{\omega\kappa} & \mathbf{K}_{\omega\omega} \end{pmatrix} \quad (\text{D.6})$$

Calculation of \mathbf{K}_{uu} , $\mathbf{K}_{u\kappa}$, $\mathbf{K}_{u\omega}$

Calculation of the first bloc line of the elementary stiffness matrix can be obtained through the derivative of \mathbf{F}_u with respect to \mathbf{u}^e , $\bar{\kappa}^e$ and $\bar{\omega}^e$:

$$\dot{\mathbf{F}}_u = \dot{\mathbf{F}}_{uu} + \dot{\mathbf{F}}_{u\kappa} + \dot{\mathbf{F}}_{u\omega} = \mathbf{K}_{uu} \cdot \dot{\mathbf{u}}_e + \mathbf{K}_{u\kappa} \cdot \dot{\bar{\kappa}}^e + \mathbf{K}_{u\omega} \cdot \dot{\bar{\omega}}^e \quad (\text{D.7})$$

Derivation of $\dot{\mathbf{F}}_u$ leads to:

$$\dot{\mathbf{F}}_u = \int_{\Omega_0^e} J \dot{\mathbf{B}}_L^T \cdot \{\boldsymbol{\Sigma}\} + J \mathbf{B}_L^T \cdot \{\dot{\boldsymbol{\Sigma}}\} + \dot{J} \mathbf{B}_L^T \cdot \{\boldsymbol{\Sigma}\} \, d\Omega_0 \quad (\text{D.8})$$

In the central term, the derivative tensor $\dot{\boldsymbol{\Sigma}}$ can be separated into three parts corresponding to variations relative to the different unknowns:

$$\dot{\boldsymbol{\Sigma}} = \dot{\boldsymbol{\Sigma}}_u + \dot{\boldsymbol{\Sigma}}_\kappa + \dot{\boldsymbol{\Sigma}}_\omega \quad (\text{D.9})$$

The calculation of \mathbf{K}_{uu} follows usual derivations for finite strain formulation and leads to:

$$\mathbf{K}_{uu} = \int_{\Omega^e} \mathbf{B}_D^T \cdot \{\mathbb{C}^\tau\} \cdot \mathbf{B}_D \, d\Omega + \int_{\Omega^e} \mathbf{B}_L^T \cdot \mathbf{M}_R(\boldsymbol{\Sigma}) \cdot \mathbf{B}_L \, d\Omega = \mathbf{K}_{uu}^M + \mathbf{K}_{uu}^G \quad (\text{D.10})$$

where \mathbf{K}_{uu}^M is the part related to the material non-linearity and \mathbf{K}_{uu}^G is the geometrical non-linearity.

Then, to compute the $\mathbf{K}_{u\kappa}$ term, let us focus on the part of the derivative of $\boldsymbol{\Sigma}$ that depends on $\bar{\kappa}$:

$$\dot{\boldsymbol{\Sigma}}_\kappa = \frac{\partial \Delta \boldsymbol{\Sigma}}{\partial \Delta \bar{\kappa}} \dot{\bar{\kappa}} \quad (\text{D.11})$$

The corresponding variation of \mathbf{F}_u is:

$$\dot{\mathbf{F}}_{u\kappa} = \int_{\Omega_0^e} J \mathbf{B}_L^T \cdot \{\dot{\boldsymbol{\Sigma}}_\kappa\} \, d\Omega_0 = \int_{\Omega_0^e} J \mathbf{B}_L^T \cdot \left\{ \frac{\partial \boldsymbol{\Sigma}}{\partial \bar{\kappa}} \right\} (\mathbf{N} \cdot \dot{\bar{\kappa}}^e) \, d\Omega_0 \quad (\text{D.12})$$

so that:

$$\mathbf{K}_{u\kappa} = \int_{\Omega^e} \left(\mathbf{B}_D^T \cdot \left\{ \frac{\partial \Sigma}{\partial \bar{\kappa}} \right\} \right) \otimes \mathbf{N} \, d\Omega \quad (\text{D.13})$$

where $\frac{\partial \Sigma}{\partial \bar{\kappa}}$ is computed using a sub block matrix of the consistent tangent matrix \mathbf{K}^{mat} (eq. B.4) as :

$$\frac{\partial \Sigma}{\partial \bar{\kappa}} = \left. \frac{\partial \sigma}{\partial \bar{\kappa}} \right|^\diamond \quad (\text{D.14})$$

The bloc $\mathbf{K}_{u\omega}$ is computed in a similar way by replacing $\bar{\kappa}$ by $\bar{\omega}$ from equation D.11 to equation D.14.

Calculation of $\mathbf{K}_{\kappa u}$, $\mathbf{K}_{\kappa \kappa}$, $\mathbf{K}_{\kappa \omega}$

Calculation of the second bloc line can be obtained by writing the variation of \mathbf{F}_κ :

$$\begin{aligned} \dot{\mathbf{F}}_\kappa &= \int_{\Omega_0^e} J(\dot{\bar{\kappa}} - \dot{\kappa}) \mathbf{N} + J l_\kappa^2 \left(\dot{\mathbf{G}}^T \cdot \mathbf{G} + \mathbf{G}^T \cdot \dot{\mathbf{G}} \right) \cdot \bar{\boldsymbol{\kappa}}^e + J l_\kappa^2 \mathbf{G}^T \cdot \mathbf{G} \cdot \dot{\bar{\boldsymbol{\kappa}}}^e \\ &\quad + \dot{J} \left((\bar{\kappa} - \kappa) \mathbf{N} + l_\kappa^2 \mathbf{G}^T \cdot \mathbf{G} \cdot \bar{\boldsymbol{\kappa}}^e \right) \, d\Omega_0 \end{aligned} \quad (\text{D.15})$$

and considering the derivative $\dot{\kappa}$ as the sum of the partial derivative of κ regarding the variables \mathbf{u}^e , $\bar{\boldsymbol{\kappa}}^e$ and $\bar{\boldsymbol{\omega}}^e$:

$$\dot{\kappa} = \dot{\kappa}_u + \dot{\kappa}_\kappa + \dot{\kappa}_\omega \quad (\text{D.16})$$

The term $\mathbf{K}_{\kappa u}$ is the most complex of the three terms to calculate. Indeed it requires to calculate the derivative of $\dot{\mathbf{F}}_\kappa$ with respect to the displacements, which involves three terms: $-J\dot{\kappa}\mathbf{N}$, $Jl_\kappa^2(\dot{\mathbf{G}}^T \cdot \mathbf{G} + \mathbf{G}^T \cdot \dot{\mathbf{G}}) \cdot \bar{\boldsymbol{\kappa}}^e$ and $\dot{J}((\bar{\kappa} - \kappa)\mathbf{N} + l_\kappa^2 \mathbf{G}^T \cdot \mathbf{G} \cdot \bar{\boldsymbol{\kappa}}^e) \stackrel{\text{def}}{=} \dot{J}\mathbf{T}_\kappa$.

Considering the first term, one has:

$$-J\dot{\kappa}_u \mathbf{N} = -J \left\{ \left. \frac{\partial \Delta \kappa}{\partial \Delta \boldsymbol{\varepsilon}} \right|^\diamond \right\} \cdot \mathbf{B}_D \cdot \dot{\mathbf{u}}^e$$

To compute the second term, one first notices that $\mathbf{G} = \mathbf{F}^{-T} \cdot \mathbf{G}^0$ (note that in this case, the Voigt notation is not used). Therefore

$$\dot{\mathbf{G}} = \overline{\mathbf{F}^{-T}} \cdot \mathbf{G}^0$$

remembering that $\overline{\dot{\mathbf{F}}^{-T}} = -\mathbf{L}^T \cdot \mathbf{F}^{-T}$

$$\dot{\mathbf{G}} = -\mathbf{L}^T \cdot \mathbf{F}^{-T} \cdot \mathbf{G}^0 = -\mathbf{L}^T \cdot \mathbf{G} \quad \text{and} \quad \dot{\mathbf{G}}^T = -\mathbf{G}^T \cdot \mathbf{L}$$

Let \mathcal{V} be the operator linking the Voigt representation of a tensor to the matrix representation such that

$$\mathbf{a} = \mathcal{V} \cdot \{\mathbf{a}\} \quad \text{or} \quad a_{ij} = \mathcal{V}_{ijk} a_k$$

and \mathcal{V}^* such that $\mathbf{a}^T = \mathcal{V}^* \cdot \{\mathbf{a}\}$. Indeed $\mathcal{V}^*_{ijk} = \mathcal{V}_{jik}$. Using this notation,

$$\begin{aligned} \mathbf{G}^T \cdot \dot{\mathbf{G}} \cdot \bar{\boldsymbol{\kappa}}^e &= -\mathbf{G}^T \cdot \mathbf{L}^T \cdot \mathbf{G} \cdot \bar{\boldsymbol{\kappa}}^e = -\mathbf{G}^T \cdot (\mathcal{V}^* \cdot (\mathbf{B}_L \cdot \dot{\mathbf{u}}^e)) \cdot \mathbf{G} \cdot \bar{\boldsymbol{\kappa}}^e \\ &= -\mathbf{G}^T \cdot (\mathcal{V}^* \cdot (\mathbf{B}_L \cdot \dot{\mathbf{u}}^e)) \cdot \vec{\nabla} \bar{\boldsymbol{\kappa}} \\ G_{ij}^T \dot{G}_{jn} \bar{\kappa}_n^e &= -G_{ij}^T V_{jkl}^* B_{lm}^L \dot{u}_m^e \nabla_k \bar{\kappa} = -G_{ij}^T V_{kjl} B_{lm}^L \dot{u}_m^e \nabla_k \bar{\kappa} \\ &= -G_{ij}^T \nabla_k \bar{\kappa} V_{kjl} B_{lm}^L \dot{u}_m^e \\ \mathbf{G}^T \cdot \dot{\mathbf{G}} \cdot \bar{\boldsymbol{\kappa}}^e &= -\mathbf{G}^T \cdot (\vec{\nabla} \bar{\boldsymbol{\kappa}} \cdot \mathcal{V} \cdot \mathbf{B}_L) \cdot \mathbf{u}^e \end{aligned}$$

Similarly

$$\dot{\mathbf{G}}^T \cdot \mathbf{G} \cdot \bar{\boldsymbol{\kappa}}^e = -\mathbf{G}^T \cdot (\vec{\nabla} \bar{\boldsymbol{\kappa}} \cdot \mathcal{V}^* \cdot \mathbf{B}_L) \cdot \dot{\mathbf{u}}_m^e$$

and

$$\begin{aligned} \dot{\mathbf{G}}^T \cdot \mathbf{G} \cdot \bar{\boldsymbol{\kappa}}^e + \mathbf{G}^T \cdot \dot{\mathbf{G}} \cdot \bar{\boldsymbol{\kappa}}^e &= -\mathbf{G}^T \cdot (\vec{\nabla} \bar{\boldsymbol{\kappa}} \cdot (\mathcal{V} + \mathcal{V}^*) \cdot \mathbf{B}_L) \cdot \dot{\mathbf{u}}^e \\ &= -2\mathbf{G}^T \cdot (\vec{\nabla} \bar{\boldsymbol{\kappa}} \cdot \mathcal{V} \cdot \mathbf{B}_D) \cdot \dot{\mathbf{u}}^e \end{aligned}$$

Finally, one now considers the last term $\dot{J} \mathbf{T}_k$.

$$\dot{J} \mathbf{T}_k = J \text{trace}(\mathbf{L}) \mathbf{T}_k = J(\{\mathbf{1}\} \cdot \mathbf{B}_D \cdot \dot{\mathbf{u}}^e) \mathbf{T}_\kappa = J \mathbf{T}_\kappa \otimes (\{\mathbf{1}\} \cdot \mathbf{B}_D) \cdot \dot{\mathbf{u}}^e \quad (\text{D.17})$$

In the end, one finally gets:

$$\mathbf{K}_{\kappa u} = \int_{\Omega^e} \left(- \left\{ \frac{\partial \Delta \kappa}{\partial \Delta \boldsymbol{\varepsilon}} \right\}^\diamond - 2l_\kappa^2 \mathbf{G}^T \cdot (\vec{\nabla} \bar{\boldsymbol{\kappa}} \cdot \mathcal{V}) + \mathbf{T}_\kappa \otimes \{\mathbf{1}\} \right) \cdot \mathbf{B}_D \, d\Omega \quad (\text{D.18})$$

where $\left. \frac{\partial \Delta \kappa}{\partial \Delta \boldsymbol{\varepsilon}} \right|^\diamond$ is computed using a sub block matrix of the consistent tangent matrix \mathbf{K}^{mat} (eq. B.4) as:

$$\left. \frac{\partial \Delta \kappa}{\partial \Delta \boldsymbol{\varepsilon}} \right|^\diamond = \mathbf{Q} \cdot \frac{\partial \Delta \kappa}{\partial \Delta \boldsymbol{\varepsilon}} \cdot \mathbf{Q}^T \quad (\text{D.19})$$

Calculation of the term $\mathbf{K}_{\kappa\kappa}$ is more direct:

$$\mathbf{K}_{\kappa\kappa} = \int_{\Omega^e} \left(1 - \frac{\partial\kappa}{\partial\bar{\kappa}}\right) \mathbf{N} \otimes \mathbf{N} + l_\kappa^2 \mathbf{G}^T \cdot \mathbf{G} \, d\Omega \quad (\text{D.20})$$

using

$$\dot{\kappa}_\kappa = \frac{\partial\kappa}{\partial\bar{\kappa}} \dot{\bar{\kappa}} = \frac{\partial\kappa}{\partial\bar{\kappa}} \mathbf{N} \cdot \dot{\bar{\kappa}}^e$$

Similarly, one has:

$$\mathbf{K}_{\kappa\omega} = \int_{\Omega^e} -\frac{\partial\kappa}{\partial\bar{\omega}} \mathbf{N} \otimes \mathbf{N} \, d\Omega \quad (\text{D.21})$$

using

$$\dot{\kappa}_\omega = \frac{\partial\kappa}{\partial\bar{\omega}} \dot{\bar{\omega}} = \frac{\partial\kappa}{\partial\bar{\omega}} \mathbf{N} \cdot \dot{\bar{\omega}}^e$$

Calculation of $\mathbf{K}_{\omega\omega}$, $\mathbf{K}_{\omega\kappa}$, $\mathbf{K}_{\omega\omega}$

Calculation of the last bloc line can be obtained exactly in the same way as the second bloc line by writing the variation of \mathbf{F}_ω . It leads to the same terms only replacing κ by ω .

References

- Ait-Amokhtar, H., Vacher, P., Boudrahem, S., 2006. Kinematics fields and spatial activity of Portevin–Le Chatelier bands using the digital image correlation method. *Acta Mater.* 54, 4365–4371.
- Aldakheel, F., Wriggers, P., Miehe, C., 2018. A modified gurson-type plasticity model at finite strains: formulation, numerical analysis and phase-field coupling. *Computational Mechanics* 62 (4), 815–833.
- Ambati, M., Gerasimov, T., De Lorenzis, L., 2015. Phase-field modeling of ductile fracture. *Comput. Mech.* 55, 1017–1040.
- Ambati, M., Kruse, R., De Lorenzis, L., 01 2016. A phase-field model for ductile fracture at finite strains and its experimental verification. *Comput. Mech.* 57.
- Bazant, Z., Pijaudier-Cabot, G., 1988. Non local continuum damage. localization, instability and convergence. *J. Applied Mech.* 55, 287–294.
- Benzerga, A., Besson, J., 2001. Plastic potentials for anisotropic porous solids. *Eur. J. Mech./A* 20A (3), 397–434.

- Benzerga, A., Leblond, J.-B., 2010. Ductile Fracture by Void Growth to Coalescence. *Advances in Applied Mechanics* 44, 169–305.
- Besson, J., 2009. Damage of ductile materials deforming under multiple plastic or viscoplastic mechanisms. *Int. J. Plasticity* 25, 2204–2221.
- Besson, J., McCowan, C., Drexler, E., 2013. Modeling flat to slant fracture transition using the computational cell methodology. *Eng. Fract. Mech.* 104, 80–95.
- Besson, J., Steglich, D., Brocks, W., 2001. Modeling of crack growth in round bars and plane strain specimens. *Int. J. Solids Structures* 38 (46–47), 8259–8284.
- Besson, J., Steglich, D., Brocks, W., 2003. Modeling of plane strain ductile rupture. *Int. J. Plasticity* 19 (10), 1517–1541.
- Borden, M., Hughe, T., Landis, C., Anvari, A., Lee, I., 2016. A phase-field formulation for fracture in ductile materials: Finite deformation balance law derivation, plastic degradation, and stress triaxiality effects. *Comp. Meth. Appl. Mech. Engng* 312, 130–166.
- Brepols, T., Wulfinghoff, S., Reese, S., 2017. Gradient-extended two-surface damage-plasticity: Micromorphic formulation and numerical aspects. *Int. J. Plasticity* 97, 64–106.
- Bron, F., Besson, J., Pineau, A., 2004. Ductile rupture in thin sheets of two grades of 2024 aluminum alloy. *Mater. Sci. Engng A* 380, 356–364.
- Chen, Y., Lorentz, E., Besson, J., 2020. Properties of a nonlocal GTN model within the context of small—scale yielding. *Int. J. Plasticity*, 102701.
- Chu, C., Needleman, A., 1980. Void nucleation effects in biaxially stretched sheets. *J. Engng Mater. Technol.* 102, 249–256.
- Diamantopoulou, E., Liu, W., Labergere, C., Badreddine, H., Saanouni, K., Hu, P., 2017. Micromorphic constitutive equations with damage applied to metal forming. *Int. J. Damage Mech.* 26 (2), 314–339.
- Dittmann, M., Aldakheel, F., Schulte, J., Schmidt, F., Krüger, M., Wriggers, P., C., H., 2020. Phase-field modeling of porous-ductile fracture in non-linear thermo-elasto-plastic solids. *Comp. Meth. Appl. Mech. Engng* 361, 112730.

- Eldahshan, H., Bouchard, P.-O., Alves, J., Perchat, E., Pino Munoz, D., Mar. 2021. Phase field modeling of ductile fracture at large plastic strains using adaptive isotropic remeshing. *Computational Mechanics* 67 (3), 763–783.
- Enakoutsa, K., Leblond, J., Perrin, G., 2007. Numerical implementation and assessment of a phenomenological nonlocal model of ductile rupture. *Comp. Meth. Appl. Mech. Engng* 196 (13-16), 1946–1957.
- Engelen, R., Geers, M., Baaijens, F., 2003. Nonlocal implicit gradient-enhanced elasto-plasticity for the modelling of softening behaviour. *Int. J. Plasticity*, 403–433.
- Forest, S., 2009. Micromorphic approach for gradient elasticity, viscoplasticity, and damage. *J. Eng. Mech.* 135, 117–131.
- Francfort, G., Marigo, J.-J., 1998. Revisiting brittle fracture as an energy minimization problem. *J. Mech. Phys. Solids* 46 (8), 1319–1342.
- Geers, M., de Borst, R., Brekelmans, W., Peerlings, R., 1998. Strain-based transient-gradient damage model for failure analyses. *Comp. Meth. Appl. Mech. Engng* 160, 133–153.
- Gorodetskyi, P., Hütter, M., Geers, M., 2017. Detecting precursors of localization by strain-field analysis. *Mech. Mater.* 110, 84–97.
- Heider, Y., Markert, B., 2017. A phase-field modeling approach of hydraulic fracture in saturated porous media. *Mech. Res. Commun.* 80, 38–46.
- Hofacker, M., Miehe, C., Nov 2012. Continuum phase field modeling of dynamic fracture: variational principles and staggered FE implementation. *Int. J. Frac.* 178 (1), 113–129.
- Hu, T., Talamini, B., Stershic, A. J., Tupek, M. R., Dolbow, J. E., 2021. A variational phase-field model For ductile fracture with coalescence dissipation. *Comput. Mech.* 68 (2), 311–335.
- Huespe, A. E., Needleman, A., Oliver, J., Sánchez, P. J., 2009. A finite thickness band method for ductile fracture analysis. *Int. J. Plasticity* 25 (12), 2349–2365.
- Huespe, A. E., Needleman, A., Oliver, J., Sanchez, P. J., 2012. A finite strain, finite band method for modeling ductile fracture. *Int. J. Plasticity* 28 (1), 53–69.

- Huetter, G., 2017. A micromechanical gradient extension of gurson's model of ductile damage within the theory of microdilational media. *Int. J. Solids Structures* 110-111, 15–23.
- Hütter, G., Linse, T., Mühlich, U., Kuna, M., 2013. Simulation of ductile crack initiation and propagation by means of a non-local Gurson-model. *Int. J. Solids Structures* 50, 662–671.
- Javani, H., Peerlings, R., Geers, M., 2016. Three-dimensional finite element modeling of ductile crack initiation and propagation. *Adv. Model. and Simul. in Eng. Sci.*, 3–19.
- Labergere, C., Guelorget, B., Francois, M., 2014. Strain rate distribution and localization band width evolution during tensile test. *Int. J. Solids Structures* 51, 3944–3961.
- Leclerc, J., Nguyen, V., Pardoën, T., Noels, L., 2020. A micromechanics-based non-local damage to crack transition framework for porous elastoplastic solids. *Int. J. Plasticity* 127.
- Linse, T., Hütter, G., Kuna, M., 2012. Simulation of crack propagation using a gradient-enriched ductile damage model based on dilatational strain. *Eng. Fract. Mech.* 95, 13–28.
- Liu, Y., Murakami, S., Kanagawa, Y., 1994. Mesh-dependence and stress singularity in finite element analysis of creep crack growth by continuum damage mechanics approach. *Eur. J. Mech./A* 13A (3), 395–417.
- Lorentz, E., Andrieux, S., 1999. A variational formulation for nonlocal damage models. *Int. J. Plasticity* 15 (2), 119–138.
- Maziere, M., Besson, J., Forest, S., Tanguy, B., Chalons, H., Vogel, F., 2010. Numerical aspects in the finite element simulation of the Portevin-Le Chatelier effect. *Comp. Meth. Appl. Mech. Engng* 199 (9-12), 734–754.
- Mediavilla, J., Peerlings, R., Geers, M., 2006. A nonlocal triaxiality-dependent ductile damage model for finite strain plasticity. *Comp. Meth. Appl. Mech. Engng* 195, 4617–4634.
- Miehe, C., Aldakheel, F., Raina, A., 2016. Phase field modeling of ductile fracture at finite strains: A variational gradient-extended plasticity-damage theory. *Int. J. Plasticity* 84, 1–32.

- Miehe, C., Hofacker, M., Schänzel, L.-M., Aldakheel, F., 2015. Phase field modeling of fracture in multi-physics problems. Part II. Coupled brittle-to-ductile failure criteria and crack propagation in thermo-elastic–plastic solids. *Comp. Meth. Appl. Mech. Engng* 294, 486–522.
- Miehe, C., Hofacker, M., Welschinger, F., 2010. A phase field model for rate-independent crack propagation: Robust algorithmic implementation based on operator splits. *Comp. Meth. Appl. Mech. Engng* 199 (45), 2765–2778.
- Nguyen, V.-D., Pardoen, T., Noels, L., 2020. A nonlocal approach of ductile failure incorporating void growth, internal necking, and shear dominated coalescence mechanisms. *J. Mech. Phys. Solids* 137, 103891.
- Peerlings, R., De Borst, R., Brekelmans, W., De Vree, J., Spee, I., 1996. Some observations on localisation in non-local and gradient damage models. *Eur. J. Mech./A* 15A (6).
- Pijaudier-Cabot, G., Bazant, Z. P., 1987. Nonlocal damage theory. *J. Engrg. Mech.* 113, 1512–1533.
- Pineau, A., Benzerga, A. A., Pardoen, T., 2016. Failure of metals I: Brittle and ductile fracture. *Acta Mater.* 107, 424–483.
- Rice, J., 1976. The localisation of plastic deformation. In: Koiter, W. (Ed.), *Proc. 14th Int. Conf. Theoretical and Applied Mechanics*, Delft. North-Holland, Amsterdam, pp. 207–220.
- Rivalin, F., 1998. Développement d’aciers pour gazoducs à haute limite d’élasticité et ténacité élevée : Mécanique et mécanismes de la rupture ductile à grande vitesse. Ph.D. thesis, École des Mines de Paris.
- Rousselier, G., 1987. Ductile fracture models and their potential in local approach of fracture. *Nucl. Eng. Des.* 105, 97–111.
- Rousselier, G., Devaux, J.-C., Mottet, G., Devesa, G., 1989. Non-Linear Fracture Mechanics, ASTM STP 995. Vol. II. American Society for Testing and Materials, Ch. A methodology for ductile fracture analysis based on damage mechanics: an illustration of a local approach of fracture, pp. 332–354.
- Scheider, I., Brocks, W., 2003. Simulation of cup-cone fracture using the cohesive model. *Eng. Fract. Mech.* 70 (14), 1943–1961.

- Seupel, A., Hütter, G., Kuna, M., 2020. On the identification and uniqueness of constitutive parameters for a non-local GTN-model. *Eng. Fract. Mech.* 229, 106817.
- Shinohara, Y., Madi, Y., Besson, J., 2016. Anisotropic ductile failure of a high-strength line pipe steel. *Int. J. Frac.* 197, 127–145.
- Sidoroff, F., Dogui, A., 2001. Some issues about anisotropic elastic-plastic models at finite strain. *Int. J. Solids Structures* 38, 9569–9578.
- Skallerud, D., Zhang, Z., 1999. Effects of finite element mesh on the numerical prediction of ductile tearing. In: *Fatigue and fracture mechanics*. ASTM STP 1332, pp. 201–214.
- Tanguy, B., Luu, T., Perrin, G., Pineau, A., Besson, J., 2008. Plastic and damage behavior of a high strength X100 pipeline steel: experiments and modelling. *Int. J. of Pressure Vessels and Piping* 85 (5), 322–335.
- Thomason, P. F., 1985a. A three-dimensional model for ductile fracture by the growth and coalescence of microvoids. *Acta Metall.* 33 (6), 1087–1095.
- Thomason, P. F., 1985b. Three-dimensional models for the plastic limit-loads at incipient failure of the intervoid matrix in ductile porous solids. *Acta Metall.* 33 (6), 1079–1085.
- Torki, M., Benzerga, A., Leblond, J.-B., 2015. On void coalescence under combined tension and shear. *J. Applied Mech.* 82.
- Tvergaard, V., 1990. Material failure by void growth to coalescence. *Advances in Applied Mechanics* 27, 83–151.
- Tvergaard, V., Needleman, A., 1984. Analysis of the cup–cone fracture in a round tensile bar. *Acta Metall.* 32, 157–169.
- Xia, L., Shih, C. F., 1995. Ductile crack growth — I. A numerical study using computational cells with microstructurally-based length scales. *J. Mech. Phys. Solids* 43, 233–259.
- Zhang, Y., Lorentz, E., Besson, J., 2018. Ductile damage modelling with locking-free regularised gtn model. *Int. J. Numer. Meth. Engng* 113 (13), 1871–1903.
- Zhang, Z., Thaulow, C., Ødegård, J., 2000. A complete Gurson model approach for ductile fracture. *Eng. Fract. Mech.* 67 (2), 155–168.